REPORT

ENZYMOLOGY

Evolutionary drivers of thermoadaptation in enzyme catalysis

Vy Nguyen,[1]* Christopher Wilson,[1]* Marc Hoemberger,[1] John B. Stiller,[1] Roman V. Agafonov,[1] Steffen Kutter,[1] Justin English,[1] Douglas L. Theobald,[2] Dorothee Kern[1]†

With early life likely to have existed in a hot environment, enzymes had to cope with an inherent drop in catalytic speed caused by lowered temperature. Here we characterize the molecular mechanisms underlying thermoadaptation of enzyme catalysis in adenylate kinase using ancestral sequence reconstruction spanning 3 billion years of evolution. We show that evolution solved the enzyme's key kinetic obstacle—how to maintain catalytic speed on a cooler Earth—by exploiting transition-state heat capacity. Tracing the evolution of enzyme activity and stability from the hot-start toward modern hyperthermophilic, mesophilic, and psychrophilic organisms illustrates active pressure versus passive drift in evolution on a molecular level, refutes the debated activity/stability trade-off, and suggests that the catalytic speed of adenylate kinase is an evolutionary driver for organismal fitness.

As a direct manifestation of molecular kinetic energy, temperature is a fundamental evolutionary driver for chemical reactions. However, it is currently not understood how the natural evolution of catalytic efficiency responds to marked changes in environmental temperatures. Theoretically, temperatures in biological processes could range from −50°C, where cells vitrify (*1*), to +140°C, when nucleic acids spontaneously hydrolyze (*2*). Life has entrenched itself in nearly every point along this scale, including extreme psychrophiles such as the bacteria *Psychrobacter articus* living in Arctic ice veins at −20°C (*3*) and the hyperthermophile Archean *Pyrlobus fumarii* that grows at 121°C (*4*).

It is likely that early life existed in a hot environment. The hot-start hypothesis is supported by several lines of evidence, including the presence of thermophilic organisms on the branches closest to the roots of the universal tree of life (*5*), the ratio of oxygen and silica isotopes in sedimentary chert and surrounding seawater (*6*), lower-viscosity seawater during the Archean eon (*7*), and reconstruction of ancestral proteins showing that the oldest nodes in phylogenetic trees are the most thermophilic (*8*, *9*). The hot-start hypothesis implies that life had to adapt to cooler temperatures due to cooling of the Earth. What does this temperature adaptation mean for enzymes? Enzymes had to contend with the evolutionary pressures on stability and activity. Chemical reaction rates, whether catalyzed or uncatalyzed, inherently scale with temperature. Hence, a hypothetical thermophilic enzyme encountering cooler environments must evolve increased catalytic activity at lower temperatures (Fig. 1A), while accommodating relaxed selection on thermostability. However, if this mesophilic ancestor, once evolved to cooler conditions, returned to a hot environment, then selection would favor an increase in melting temperature, with no pressure on its already optimized catalytic activity (Fig. 1A).

Although intense experimental effort has gone into understanding protein thermostability (*8*, *10*, *11*), the challenge of evolving efficient enzymatic turnover at lower temperatures has not been addressed. Indeed, Wolfenden and colleagues raised this question as a crucial evolutionary obstacle (*12*, *13*). The authors reasoned that in an early hot environment, primordial chemical reactions could occur readily, but would become slow at lower temperatures because of their steep temperature dependencies (*12*, *13*). They suggested that enzymes solved the thermal kinetic obstacle at lower temperatures by decreasing the enthalpic activation barrier ($\Delta H^{\ddagger}$), resulting in a shallower temperature dependence (Fig. 1B) (*12*, *13*). Here we investigate the molecular mechanisms underlying thermoadaptation of enzyme catalysis using ancestral sequence reconstruction (ASR) spanning about 3 billion years of evolution.

ASR [reviewed in (*14*)] is a valuable tool for experimentally testing molecular evolutionary questions. ASR uses genetic patterns stored in the sequences of extant proteins, and the phylogenetic relationships between them, to infer sequences of ancestors along an evolutionary trajectory. We focused on the enzyme adenylate kinase (Adk) because it is an essential enzyme found in nearly every life form, it has a strong correlation between organismal growth temperature and Adk stability (*15*, *16*), and its catalytic mechanism is well understood (Fig. 1, C and D). Adk catalyzes the reversible conversion of Mg/adenosine 5′-triphosphate (Mg/ATP) and adenosine 3′,5′-monophosphate (AMP) into two adenosine 5′-diphosphate (ADP) molecules, maintaining nucleotide concentrations in the cell.

The phylum Firmicutes is an ancient bacterial lineage [~3 billion years ago (bya)], and its contemporary species inhabit a wide range of environments (*17*), including aerobic deep polar sediment (*Bacillus marinus*), hot thermal springs (*B. stearothermophilus*), and common soil (*B. subtilis*), as well as hot anaerobic environments such as seafloor hydrothermal vents (*C. subterraneus*) (Fig. 2A). In addition, modern Firmicutes have a particularly well-conserved core genome and slow mutational rates (*5*, *17*). A robust coestimated phylogeny and alignment of modern Firmicute Adk sequences from the National Center for Biotechnology Information database was constructed using BAli-Phy (*18*) (Fig. 2A, figs. S1 and S2, and data file S1). The strength of the reconstructed phylogeny and alignment is illustrated by strong posterior probabilities along branch sites (fig. S1) and its topological resemblance with previously reported trees based on 16 genes found in all three domains of life (*5*).

We reconstructed eight nodes along the lineage from the oldest ancestor corresponding to the divergence of aerobic and anaerobic Firmicutes, estimated divergence between 3 and 2.6 bya (*17*, *19*), toward modern-day thermophilic (*B. stearothermophilus*, *C. subterraneus*), mesophilic (*B. subtilis*), and psychrophilic (*B. marinus*) Adks (Fig. 2A and figs. S1 and S2). The great majority of sites in the reconstructed sequences have >0.95 posterior probability (fig. S3). As an independent control for phylogenetic uncertainty and proposed biases with maximum likelihood–based reconstructions (*20*), three of the nodes (ANC1, ANC3, ANC4) were also predicted using sequences sampled from the posterior distribution inferred during the BAli-phy run. Those nodes had properties nearly identical to those predicted from maximum likelihood (table S1), thus confirming that the reconstructed sequences are robust to the uncertainty inherent in the methods. Eight ancestral and four modern Adk enzymes were overexpressed in *Escherichia coli* and purified. All ancestors are active enzymes with k_{cat} values comparable to those of their modern descendants (table S2), even though they contained up to 47 amino acid differences (ANC1) relative to any modern Adk.

First, we characterized the evolutionary trajectories of melting temperatures using differential scanning calorimetry (DSC) (Fig. 2A). ANC1 starts with the highest melting temperature (T_m) of 89°C. Melting temperatures gradually decrease along the tree from the oldest reconstructed enzyme toward modern-day mesophilic and psychrophilic enzymes. In one branch, the modern thermophile *B. stearothermophilus* reevolved thermostability from an ancestor that had adopted to cooler climates (ANC6, T_m 64°C).

To view this evolutionary path through a structural lens, we solved high-resolution crystal

[1]Howard Hughes Medical Institute and Department of Biochemistry, Brandeis University, Waltham, MA 02452, USA. [2]Department of Biochemistry, Brandeis University, Waltham, MA 02452, USA.
*These authors contributed equally to this work.
†Corresponding author. Email: dkern@brandeis.edu

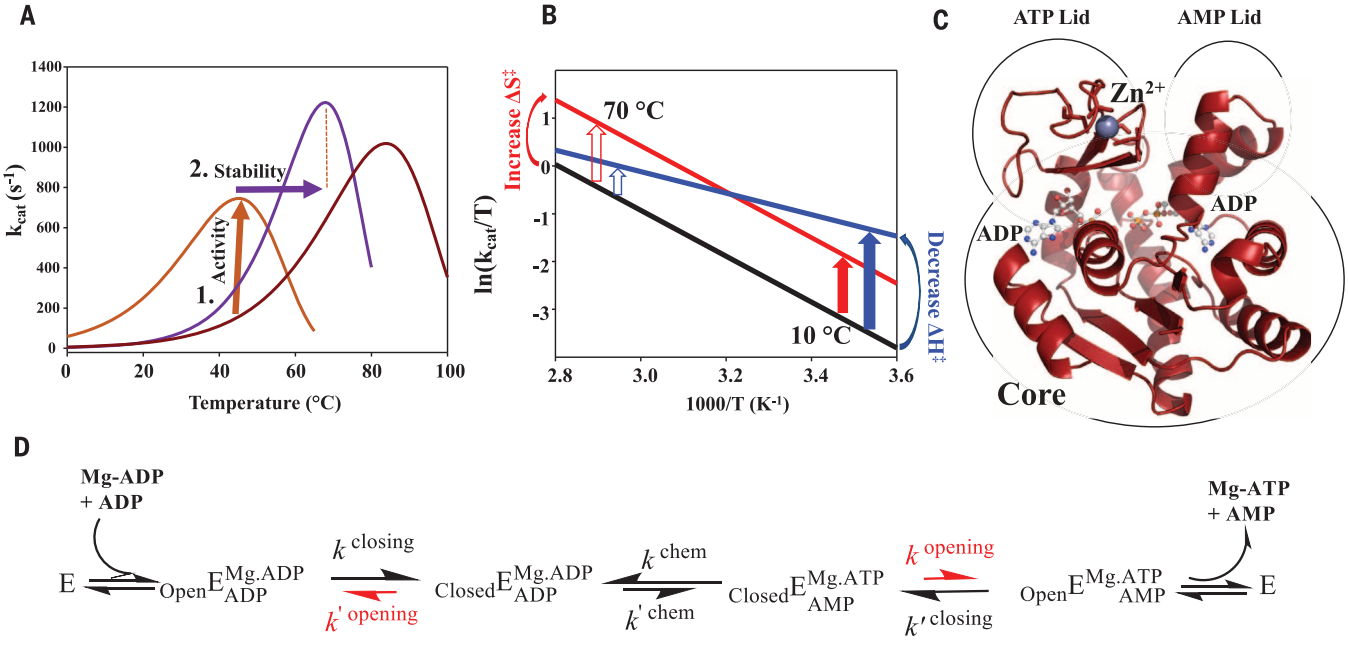

Fig. 1. Evolutionary pressures on enzymes during adaptation to environmental temperature changes. (**A**) Hypothetical ancestral protein (dark red) needs to increase activity at lower temperatures (brown arrow), resulting in a second ancestral enzyme (brown). Evolution from cold to hot imposes pressure on increased stability (purple arrow), resulting in a modern thermophile (purple). (**B**) Eyring plot illustrating proposed mechanisms for increasing enzymatic activity at colder temperatures by increasing $\Delta S^{\ddagger}$ (red) versus decreasing $\Delta H^{\ddagger}$ (blue) relative to the uncatalyzed reaction (black) (*12*, *13*, *34*) with larger rate acceleration at low temperatures by $\Delta H^{\ddagger}$ (blue arrow). (**C**) The 1.2 Å x-ray structure of ANC1 Adk with two ADPs bound. (**D**) Reaction scheme for Adk catalysis, highlighting lid opening as the rate-limiting step (red) [from (*22*)].

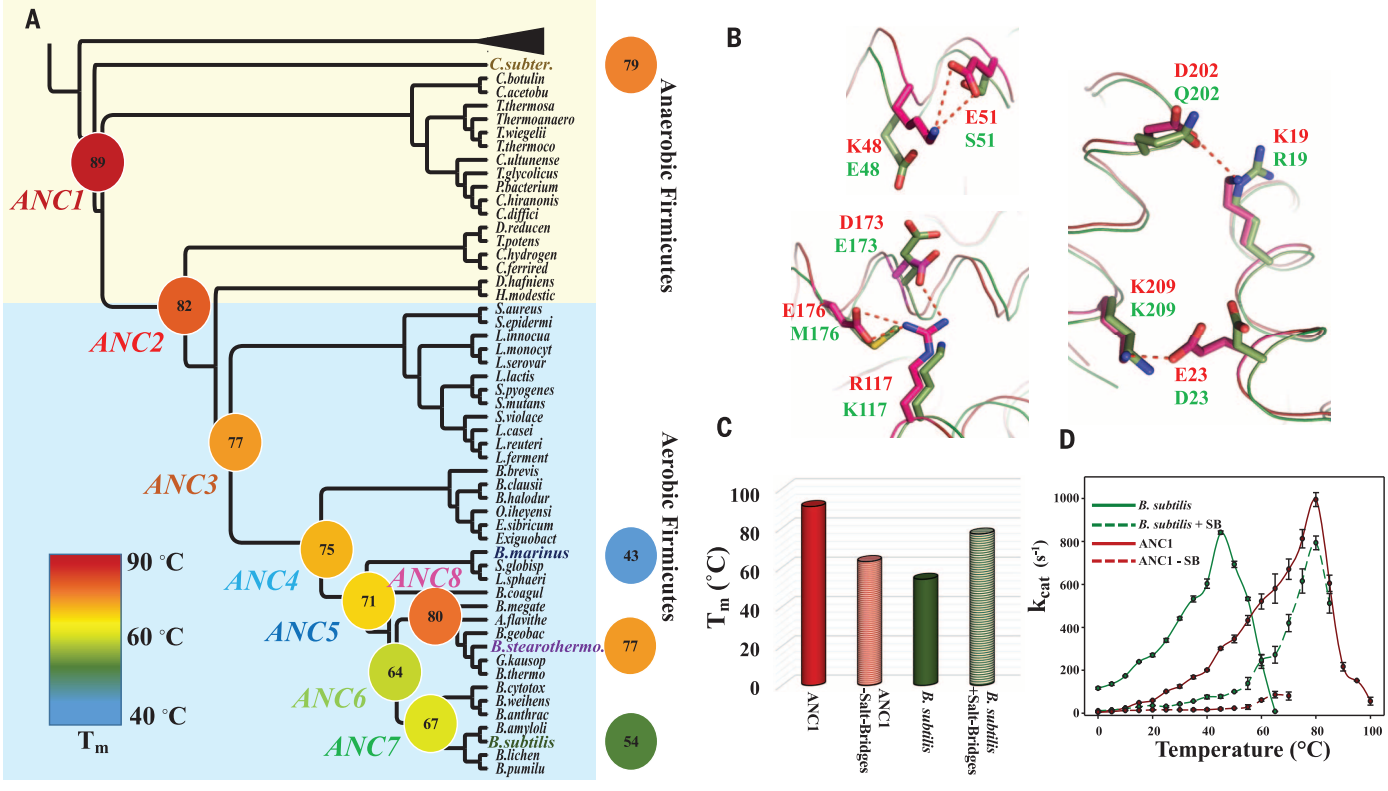

Fig. 2. Evolution of thermostability through the reconstructed Adk phylogeny spanning 2.5 to 3 bya. (**A**) Collapsed cladogram of the tree (see fig. S1) used to resurrect ancestral Adks (nomenclature and colors for the 12 Adks are used throughout the manuscript). Measured T_ms are indicated and illustrated by a continuous color scale. (**B**) Superposition of ANC1 (red, 5G3Y) and *B. subtilis* Adk (green, 1P3J) structures suggests salt bridges (dotted red lines) in ANC1 responsible for high T_m. (**C**) Removing these salt bridges from ANC1 or adding them into *B. subtilis* results in a drastic decrease or increase in T_m, respectively. (**D**) Corresponding activity changes of these mutant proteins. Errors are standard errors from the linear fit based on eight time points for each temperature.

structures of ANC1, ANC3, and ANC4 bound to ADP or the substrate analog Ap5A [P1, P5-di(adenosine-5′) pentaphosphate] (table S3). A global comparison of our ancestor structures among each other and with crystal structures of the modern mesophilic, psychrophilic, and thermophilic Adk enzymes (1P3J, 1S3G, 1ZIN) hinted at salt bridges as the primary source for differential stabilities (Fig. 2B, fig. S4, and table S4). Several unique salt bridges sequentially disappear during evolution toward colder environments and then reappear in species that subsequently adapt to hot niches (fig. S5 and table S5). To experimentally test this mechanistic interpretation, we mutated residues responsible for the salt bridge differences in ANC1 to the corresponding residues found in Adk from *B. subtilis*, and vice versa (Fig. 2, B and C). The changes in T_m from interchanging only these five salt bridges indicate that they are indeed the primary contributors to thermostability. Both contrived "swap mutant enzymes" are catalytically impaired (Fig. 2D), indicating epistasis, meaning that the backgrounds in which these salt bridges are placed influence the effects of the mutations (*14*).

The thermostability data provided the starting point to address the question of how catalytic power evolved in response to environmental temperature change. For this purpose, catalytic rates were measured between 0° and 100°C (Fig. 3) for all 13 enzymes. First, all eight ancestors display catalytic activities at their optimal temperatures that differ by less than a factor of 3 from those of modern Adk enzymes, providing an additional internal control for accurately reconstructed sequences (*11*). Second, ancestors and modern Adk enzymes display the typical trend of increased activity with temperature followed by a steep decline due to thermal denaturation (fig. S6). Third, below 25°C, ANC1 and ANC2 have a strong temperature dependence with very low catalytic rates, agreeing with the prediction that ancient enzymes are adapted exclusively to hot environments.

To elucidate how enzymatic turnover evolved in response to temperature changes, we generated Eyring plots for each modern and ancestral Adk [see Fig. 1B as an illustration of the hypothesis put forward in (*12*, *13*)]. Unexpectedly, the oldest ancestors have positively curved Eyring plots. The curvature is less pronounced for the more recent ancestors (Fig. 3). Nonlinear Eyring plots can be trivially caused either by protein denaturation at higher temperatures or a temperature-dependent reversible inactivation equilibrium. Both possibilities were ruled out by nuclear magnetic resonance (NMR) spectra for this temperature range (fig. S7). Also, subsaturating substrate concentration due to a large increase in K_m at elevated temperatures was excluded as a potential explanation (fig. S8). Another potential source of a curved Eyring plot is a change in the rate-limiting step at different temperatures (Fig. 4A) (*21*). Because lid opening has been shown to be rate-limiting for modern Adk from various organisms, we considered that the chemical step of phosphoryl transfer might become rate-limiting at a certain temperature. However, quench flow experiments show a product burst both at low and high temperatures for ANC1, indicating a conventional rate-limiting conformational change at both temperatures following a faster phosphoryl-transfer step (Fig. 4B), in agreement with earlier work on *E. coli* and *Aquifex aeolicus* Adk (*22*). We confirmed this result by NMR relaxation

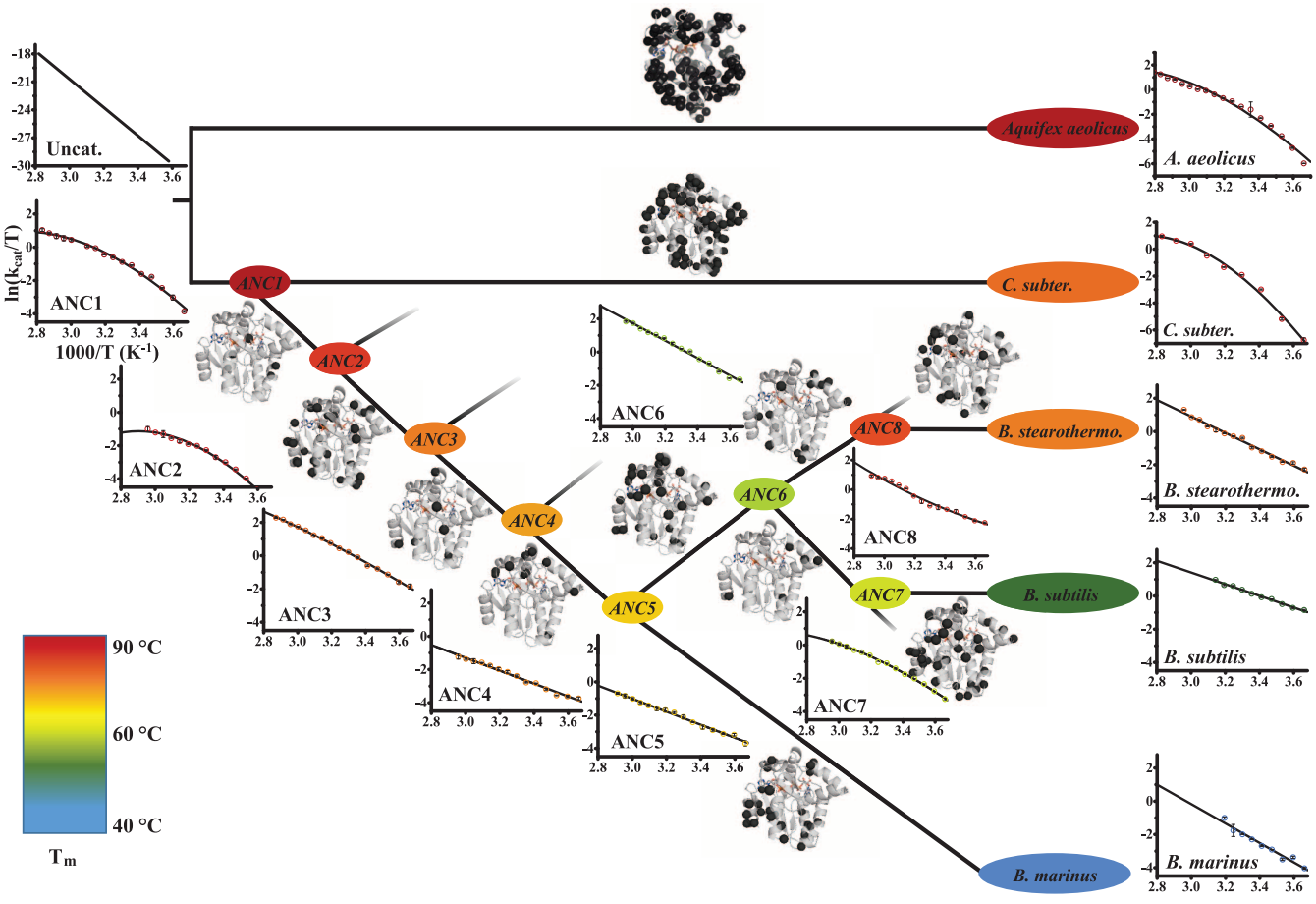

Fig. 3. Evolution of enzyme activity over about 2.5 to 3 bya. Temperature dependence of k_{cat} is shown as Eyring plots including the fits to Eq. 1, and is compared to the uncatalyzed reaction reported (*34*). T_ms are shown using color code of Fig. 2. For fitting, only data for temperatures before unfolding set in are used, with a nonzero $\Delta C_p^{\ddagger}$ term when validated by an *F* test (see fig. S6 for complete activity–temperature profiles). Along the evolutionary trajectory from ANC1 via mesophilic ANC6 to modern Adks, positive curvature evolved to straight Eyring plots. In contrast, *C. subterraneus* and *A. aeolicus* Adks retain positive curvature. Sites of mutations between the nodes are plotted as black spheres on the structure of ANC1. Error bars as in Fig. 2D.

experiments on ANC1 during catalysis (*22*), determining a lid-opening rate of 49 s^{-1} at 15°C that is within experimental error of the corresponding k_{cat} (Fig. 4C).

Having established that k_{cat} reports on lid opening over the relevant temperature range, we asked whether the curved Eyring plots arise from a nonzero change in heat capacity of activation ($\Delta C_p^{\ddagger}$; Eq. 1 is repeated in supplementary materials with all terms defined):

$$\ln\left(\frac{k_{cat}}{T}\right) = \ln\left(\frac{k_B}{h}\right) - \frac{\Delta H_{T_0}^{\ddagger} + \Delta C_p^{\ddagger}(T - T_0)}{RT} + \frac{\Delta S_{T_0}^{\ddagger} + \Delta C_p^{\ddagger} \ln(T/T_0)}{R} \quad (1)$$

$\Delta C_p^{\ddagger}$ reflects the difference in heat capacity between the transition state and the closed state, and a nonzero value necessarily imparts temperature dependence to the activation enthalpy. Fitting the activity data to such an extended model including a $\Delta C_p^{\ddagger}$ term (Eq. 1) indeed rationalizes temperature adaptation during evolution of enzyme catalysis over 3 billion years (Fig. 3). The strong negative $\Delta C_p^{\ddagger}$ of the oldest ancestors results in extremely slow catalysis at low temperatures (Figs. 3 and 4D), a tolerable situation for these hot-Earth ancestors. Notably, this kinetic obstacle to catalysis during thermoadaptation to colder environmental temperatures was removed by progressively reducing $\Delta C_p^{\ddagger}$ toward zero in evolution toward modern enzymes (Fig. 3). Tracing the $\Delta C_p^{\ddagger}$ changes along the evolutionary pathways exposes a gradual trend (Fig. 4D) of greatly increasing the catalytic rates at lower temperatures, the parameter under direct evolutionary pressure. Negative $\Delta C_p^{\ddagger}$ values produce a larger enthalpy of activation at lower temperatures, causing the severe drop in catalytic rate constants (Fig. 4D and Eq. 1).

Intriguingly, values of $\Delta C_p^{\ddagger}$ found here are comparable in magnitude to the ones measured for protein-folding kinetics (*23*). Moreover, Fersht and colleagues had speculated that $\Delta C_p^{\ddagger}$ could in principle influence enzyme catalysis for cases where conformational transitions are rate-limiting (*23*), as is shown here. Although it would be desirable to identify whether solvation of hydrophobic residues or charged residues, or differences in dynamics, are responsible for the measured $\Delta C_p^{\ddagger}$, this is unachievable because (i) the heat capacity of the transition state cannot be estimated, (ii) the $\Delta C_p^{\ddagger}$ values are small, and (iii) the molecular character of the transition state is unknown (*23*).

In summary, this thermoadaptation mechanism for catalysis differs from the original hypothesis of a uniform decrease in $\Delta H^{\ddagger}$ in the evolution of enzyme catalysis (Fig. 1B) (*12*, *13*) and creates an even larger rate acceleration at lower temperatures relative to the uncatalyzed rate. The source of rate acceleration by the oldest ancestral Adk relative to the nonenzymatic rate is indeed a decrease in $\Delta H^{\ddagger}$ (Figs. 3 and 4), as postulated by Wolfenden (*12*, *13*), but only at the high primordial temperatures. Adk evolution over the next 3 billion years encountered a decrease in the environmental temperatures and was driven by a corresponding change in the heat capacity of activation. This process resulted in comparable $\Delta H^{\ddagger}$ values for all ancestors and modern extremophiles at their corresponding optimal temperatures (Fig. 4D).

To further test our model, we characterized two additional modern hyperthermophiles,

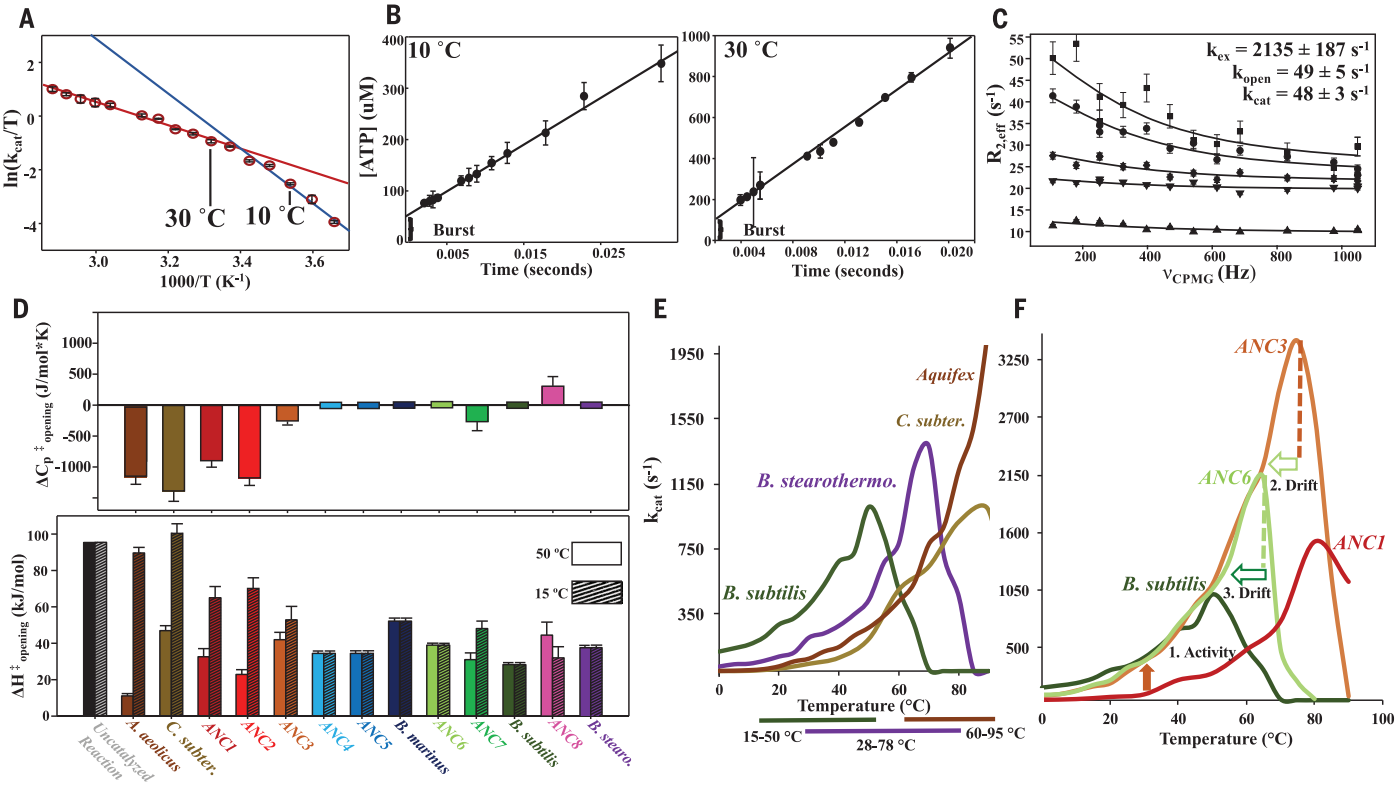

Fig. 4. Change in $\Delta C_p^{\ddagger}$ as evolutionary driver for thermoadaptation of catalysis and implications for organismal fitness. (**A**) Eyring plot of ANC1 activity with theoretical explanation of curvature caused by a change in rate-limiting step between 10° and 30°C between two steps with different temperature dependencies (red and blue lines). (**B**) Quench-flow experiment of 100 μM ANC1 and 5 mM Mg/ADP shows a burst for fast phosphoryl transfer, followed by the rate-limiting lid opening (linear part) (mean ± SEM; $N = 3$ experiments). (**C**) ^{15}N CPMG relaxation (*22*) data of representative residues of ANC1 during catalysis at saturating concentrations of Mg/ADP at 15°C. Error bars denote uncertainty in the ratio of cross-peaks, estimated as root mean square deviation from duplicates. (**D**) Heat capacity of activation for lid-opening dynamics ($\Delta C_{p\,opening}^{\ddagger}$) for all Adk enzymes determined from the data of Fig. 3 fitted to Eq. 1 (top) and corresponding $\Delta H^{\ddagger}$ values at 50° and 15°C (bottom) (standard errors in the fitted parameters). (**E**) Correlation between activity–temperature profiles of modern Adks with their known growth temperatures (*35*–*38*) (bottom bars). (**F**) Activity–temperature profiles along the evolutionary path from ANC1 to modern *B. subtilis* labeling active pressure for increased activity at lower temperatures (orange arrow from ANC1 to ANC3), creating a hyperactive and hyperstable enzyme in ANC3 and subsequently a slower passive drift to decreased stabilities via ANC6 to *B. subtilis* (light green and green open arrow).

C. subterraneus and *A. aeolicus* Adk. These organisms have apparently remained thermophilic throughout their evolutionary history (Fig. 3 and S9) and therefore never experienced sustained selection for low-temperature catalytic efficiency. As predicted by our model, both modern enzymes behave like our oldest ancestor, showing large negative $\Delta C_p^{\ddagger}$ values, in sharp contrast to hyperthermophilic *B. stearothermophilus* (Figs. 3 and 4D). The negligible $\Delta C_p^{\ddagger}$ of *B. stearothermophilus* seems to be a biophysical-vestigial leftover from its evolutionary history in a cooler environment. These results illustrate elements of "evolutionary memory," thereby resolving long-standing controversies in interpreting differences in modern extremophiles within the same enzyme class (*24*).

Starting from modern *Bacillus* Adk enzymes, Shamoo's lab demonstrated a direct link between Adk stability and organismal fitness (*15*, *16*). Comparing our in vitro Adk activity temperature profiles with known growth temperature ranges of the organisms leads to the hypothesis that a minimal catalytic rate of Adk is needed for survival (Fig. 4E). We propose that differential fitness at low temperatures is directly linked to the enzymatic rate: The survival of *B. stearothermophilus* at mesophilic temperatures is a holdover from the mesophilic sojourn taken by its ancestor, explaining its perplexingly broad organismal fitness (*25*) (Fig. 4E).

According to the view that protein stability must be sacrificed to support the conformational flexibility necessary for enzymatic activity, the marginal melting temperatures in mesophiles and psychrophiles would be an adaptive trait (*26*). We do not observe this correlation, as ANC3 is both thermostable and catalytically active at low temperatures, resulting in a "super-enzyme" with the unprecedented optimal k_{cat} among Adks of ~3500 s^{-1} (Fig. 4F). Adk is especially relevant to the flexibility/stability trade-off debate, as the rate-limiting step is a dynamic lid-opening process (*22*). With no pressure on either maintaining or losing stability, the melting temperatures of Adk enzymes likely decreased by genetic drift toward modern mesophiles and psychrophiles while the activity was maintained by purifying selection (Fig. 4F) (*26*, *27*). Our evidence against the activity/stability trade-off is immediately pertinent to biotechnology for producing very active enzymes that are also hyperstable.

How do our results compare to previous studies on the evolution of thermostability? Thermostabilities of ANC1 and ANC2 show excellent agreement with melting temperatures of ancestral beta-lactamases (89° to 90°C) at ~ 3 bya (*28*) and the thermostability of ancestors of isopropylmalate dehydrogenase along the Bacilli clade of Firmicutes over 1 bya (*11*). The evolution of Adk's T_ms over 3 bya correlates with the change in Earth's temperature as first reported for the elongation factor Tu (*8*), although those measured T_ms are in general below the estimated Earth temperatures whereas Adk's T_m values are above. These results, using different enzymes and techniques for phylogenetic inference, demonstrate the robustness and reproducibility of ASR. Notably, our results deliver the structural mechanisms for the evolution of thermostability from ancestors to modern enzymes that could not be achieved for other reconstructed systems (*8*, *11*). A comparison of only modern *B. subtilis* and *B. stearothermophilus* Adk identified salt bridges as being crucial for the observed differences in thermostability (*29*). These salt bridges differ from the ones we identified in the evolutionary trajectory, highlighting that similar strategies can be used by evolution in different ways to increase the protein stability in response to environmental pressure.

Tracing the evolution of catalytic power under thermal pressure revealed $\Delta C_p^{\ddagger}$ as the unexpected evolutionary driver for enzymatic speed. In protein chemistry, heat capacities have almost entirely been studied for the temperature dependence of thermodynamic equilibria (ΔC_p), such as between the folded and unfolded states (*30*). $\Delta C_p^{\ddagger}$ as a source of nonlinear Eyring plots had only been measured for nonenzymatic reactions (*31*) and protein folding (*23*). A nonzero $\Delta C_p^{\ddagger}$ in enzyme catalysis where conformational transitions are rate-limiting is analogous to a nonzero $\Delta C_p^{\ddagger}$ in protein folding (*23*), an idea that suggests a unified view of protein folding that includes conformational transitions within the folded ensemble (*32*, *33*). The quantitative characterization of the evolution of enzyme activity and stability exposes the action of active selection versus passive drift in evolution on a molecular level, reveals a surprising mechanism of thermoadaptation for catalysis, opposes the commonly assumed activity/stability trade-off concept, and suggests the catalytic speed of Adk as an evolutionary driver for organismal fitness.

REFERENCES AND NOTES

1. A. Clarke *et al.*, *PLOS ONE* **8**, e66207 (2013).
2. D. A. Cowan, *Trends Microbiol.* **12**, 58–60 (2004).
3. J. W. Deming, *Curr. Opin. Microbiol.* **5**, 301–309 (2002).
4. E. Blöchl *et al.*, *Extremophiles* **1**, 14–21 (1997).
5. F. D. Ciccarelli *et al.*, *Science* **311**, 1283–1287 (2006).
6. L. P. Knauth, D. R. Lowe, *Geol. Soc. Am. Bull.* **115**, 566–580 (2003).
7. P. Fralick, J. E. Carter, *Precambrian Res.* **191**, 78–84 (2011).
8. E. A. Gaucher, S. Govindarajan, O. K. Ganesh, *Nature* **451**, 704–707 (2008).
9. S. Akanuma *et al.*, *Proc. Natl. Acad. Sci. U.S.A.* **110**, 11067–11072 (2013).
10. V. A. Risso, J. A. Gavira, D. F. Mejia-Carmona, E. A. Gaucher, J. M. Sanchez-Ruiz, *J. Am. Chem. Soc.* **135**, 2899–2902 (2013).
11. J. K. Hobbs *et al.*, *Mol. Biol. Evol.* **29**, 825–835 (2012).
12. R. B. Stockbridge, C. A. Lewis Jr., Y. Yuan, R. Wolfenden, *Proc. Natl. Acad. Sci. U.S.A.* **107**, 22102–22105 (2010).
13. R. Wolfenden, *Cell. Mol. Life Sci.* **71**, 2909–2915 (2014).
14. M. J. Harms, J. W. Thornton, *Nat. Rev. Genet.* **14**, 559–571 (2013).
15. R. Couñago, Y. Shamoo, *Extremophiles* **9**, 135–144 (2005).
16. R. Couñago, S. Chen, Y. Shamoo, *Mol. Cell* **22**, 441–449 (2006).
17. A. Moreno-Letelier, G. Olmedo-Alvarez, L. E. Eguiarte, V. Souza, *Astrobiology* **12**, 674–684 (2012).
18. B. D. Redelings, M. A. Suchard, *Syst. Biol.* **54**, 401–418 (2005).
19. F. U. Battistuzzi, A. Feijao, S. B. Hedges, *BMC Evol. Biol.* **4**, 44 (2004).
20. P. D. Williams, D. D. Pollock, B. P. Blackburne, R. A. Goldstein, *PLOS Comput. Biol.* **2**, e69 (2006).
21. A. Case, R. L. Stein, *Biochemistry* **42**, 3335–3348 (2003).
22. S. J. Kerns *et al.*, *Nat. Struct. Mol. Biol.* **22**, 124–131 (2015).
23. M. Oliveberg, Y. J. Tan, A. R. Fersht, *Proc. Natl. Acad. Sci. U.S.A.* **92**, 8926–8929 (1995).
24. G. A. Petsko, *Methods Enzymol.* **334**, 469–478 (2001).
25. D. R. Zeigler, *Microbiology* **160**, 1–11 (2014).
26. R. A. Goldstein, *Proteins* **79**, 1396–1407 (2011).
27. E. Bornberg-Bauer, H. S. Chan, *Proc. Natl. Acad. Sci. U.S.A.* **96**, 10689–10694 (1999).
28. V. A. Risso *et al.*, *J. Am. Chem. Soc.* **135**, 2899–2902 (2013).
29. E. Bae, G. N. Phillips Jr., *J. Biol. Chem.* **279**, 28202–28208 (2004).
30. N. V. Prabhu, K. A. Sharp, *Annu. Rev. Phys. Chem.* **56**, 521–548 (2005).
31. C. Canepa, *Chem. Cent. J.* **5**, 22 (2011).
32. R. Nussinov, P. G. Wolynes, *Phys. Chem. Chem. Phys.* **16**, 6321–6322 (2014).
33. P. G. Wolynes, W. A. Eaton, A. R. Fersht, *Proc. Natl. Acad. Sci. U.S.A.* **109**, 17770–17771 (2012).
34. R. B. Stockbridge, R. Wolfenden, *J. Biol. Chem.* **284**, 22747–22757 (2009).
35. G. Holtmann, E. Bremer, *J. Bacteriol.* **186**, 1683–1693 (2004).
36. D. S. Nichols, P. D. Nichols, T. A. McMeekin, *Sci. Prog.* **78**, 311–348 (1995).
37. T. N. Nazina *et al.*, *Int. J. Syst. Evol. Microbiol.* **51**, 433–446 (2001).
38. R. Huber, K. O. Stetter, *Methods Enzymol.* **330**, 11–24 (2001).

ACKNOWLEDGMENTS

This work was supported by the Howard Hughes Medical Institute (HHMI); the Office of Basic Energy Sciences, Catalysis Science Program; U.S. Department of Energy award DE-FG02-05ER15699; and NIH grant GM100966 (to D.K) and NIH grants GM096053 and GM094468 (to D.L.T.). We thank the Advanced Light Source (ALS), Berkeley, CA, USA, for access to beamlines BL8.2.1 and BL8.2.2. The Berkeley Center for Structural Biology is supported in part by the National Institutes of Health, National Institute of General Medical Sciences, and the HHMI. The ALS is supported by the director, Office of Science, Office of Basic Energy Sciences, of the U.S. Department of Energy under contract DE-AC02-05CH11231. The Protein Data Bank accession codes are 5G3Y (ANC1*Zn*ADP*ADP), 5G3Z (ANC3*Zn*Mg*Ap5A), 5G40 (ANC4*Zn*AMP*ADP), and 5G41 (ANC4*Zn*Mg*Ap5A).

SUPPLEMENTARY MATERIALS

www.sciencemag.org/content/355/6322/289/suppl/DC1
Materials and Methods
Figs. S1 to S9
Tables S1 to S5
Data File S1
References (*39*–*71*)

16 June 2016; accepted 21 November 2016
10.1126/science.aah3717

www.sciencemag.org/cgi/content/full/science.aah3717/DC1

Supplementary Materials for

Evolutionary drivers of thermoadaptation in enzyme catalysis

Vy Nguyen, Christopher Wilson, Marc Hoemberger, John B. Stiller, Roman V. Agafonov, Steffen Kutter, Justin English, Douglas L. Theobald, Dorothee Kern*

*Corresponding author. Email: dkern@brandeis.edu

Published 22 December 2016 on *Science* First Release
DOI: 10.1126/science.aah3717

This PDF file includes:

Other Supplementary Materials for this manuscript includes the following:
(available at www.sciencemag.org/cgi/content/full/science.aah3717/DC1)

Data File S1 (FASTA file)

Materials and methods

Ancestral protein sequence reconstruction and resurrection

Ancestral sequence reconstruction is highly dependent on an accurate phylogeny and multiple sequence alignment. Protein sequences used in this study where originally identified by the BLASTP algorithm (*39*) using a query composed of modern day sequences from the *Bacilli, Clostridia* and *Thermoaerobacter* classes of Firmicutes against the NCBI nr (non-redundant) protein database. The results of the search were combined and duplications removed resulting in 1059 non-redundant sequences. These sequences were aligned using MAFFT (*40*). Adk shows reasonable sequence conservation across present-day Firmicutes (21.9% identical sites and 73% similarity across species) and very few insertions or deletions. Adks from bacterial organisms outside of the Firmicutes domain were selected as an outgroup. To cull the number of sequences for use in the Bayesian analysis, sequences with 75% identity and/or containing unique large truncations, insertions and/or N-C-terminal extensions were removed resulting in 71 sequences that adequately cover the Firmicutes phylum. A robust phylogeny and alignment of the 71 selected sequences was created with the software package BAli-Phy version 2.3 (*18*), which estimates the alignment and the tree simultaneously using Bayesian methodology. The BAli-Phy analysis was performed using the RS07 insertion/deletion model (*41*), LG amino acid substitution matrix (*42*), estimating equilibrium amino acid frequencies, with gamma distributed rates across sites (four categories). The LG substitution matrix was found independently by PhyML (*43*) analysis to provide the highest log-likelihood for the Adk family. Ten independent Markov chain Monte-Carlo chains were run until the average standard deviation factor (ASDF) (*44*) and potential scale reduction factors (PSRF) - 80% CI criteria (*45*) fell below 0.01 and 1.01, respectively, indicating convergence of the chains. The strength of the reconstructed phylogeny and alignment is illustrated by high posterior probabilities of bipartitions and by its topological

resemblance with previously reported phylogenetic trees based on 16 concatenated genes found in all three domains of life.

We chose to resurrect eight nodes along the lineage between the oldest ancestor corresponding to the divergence of anaerobic Firmicutes and aerobic Firmicutes (estimated divergence between 3 billion to 2.6 billion years ago (*17, 19*)) and along the pathways towards modern day thermophilic (*B. stearothermophilus*, *C. subterraneus*), mesophilic (*B. subtilis*) and psychrophilic (*B. marinus*) Adk enzymes. Ancestral sequences were inferred using the maximum likelihood method implemented in PAML (*46*), with the maximum a posteriori phylogeny and expected parameters (normalized equilibrium frequencies and gamma shape parameter) estimated during the BAli-Phy run. The great majority of sites in the reconstructed sequences have a posterior probability greater than 0.95 (Fig. S3). We also resurrected stochastically sampled enzymes from three nodes (ANC1, ANC3, ANC4) to account for phylogenetic uncertainty and proposed biases with maximum probability reconstructions (*20*). The resurrected sampled ancestors had nearly identical properties (Table S1) as the maximum probability resurrected proteins, providing confidence that our analysis is robust to uncertainty in the reconstructed sequences.

Protein expression and purification

Contemporary and ancestral sequence cDNAs were optimized for *E. coli* expression and synthesized by Genscript. Ancestral and extant inserts were sub-cloned into pET-17b vector with a TEV cleavage site and His_6-tag on the C-terminus. Cells were grown in LB media to an OD of 0.8 before induction with 1 mM of IPTG for 6 hours at 37 °C. Adk from *B. marinus* were overexpressed at 20 °C for 18 hours with 500 μM of IPTG. Cells were lysed in the presence of benzonase by sonication. After purification via a Ni-NTA column, the His-tagged Adks were cleaved with His-tagged TEV-protease overnight at 4 °C while dialyzing against buffer 50 mM Tris-HCl pH 7.5, 200 mM NaCl, 1 mM BME. Cleaved sample was collected and run over Ni-

NTA column to remove His-tagged TEV, His tags and uncleaved His-tagged Adk contaminants. Flow-through was collected, concentrated to 5 mL and passed over a 26/600 S-75 gel filtration column. All columns were run at 4 °C.

Determination of melting temperatures

All Adk enzymes' thermostability were measured by differential thermal scanning calorimetry (DSC) VP-DSC (MicroCal). Degased enzyme solutions of 50 uM in 100 mM HEPES, 50mM NaCl pH 7.0 and a reference sample of the same buffer were scanned at 1 °C/min from 20 to 110 °C. Data were fitted to a 2-state model using the accompanying MicroCal Origin v7.

Temperature dependence enzyme kinetic assay and data analysis

Temperature dependence kinetic assays were performed over a temperature range of 0 – 100 °C in increments of 5 °C. The assays were done under ambient pressure in 50 mM MOPS, 80 mM KCl, 0.3 mg/mL BSA, pH 7.0. The enzyme solutions (final concentration varied between 0.5 nM and 300 nM) were incubated at the selected temperature for 3 minutes before MgADP (final concentration was 4 mM) was added to the enzyme. Eight time points were collected for an 8-minute reaction at each temperature. For each time point, the reaction was quenched with 10% TCA in a 1:1 ratio, spun down using Spin-X centrifugal tube filters (Costar) and then neutralized with 1.5 M HEPES, 75 mM EDTA, pH 8.0. The amount of product produced at each time point was analyzed on a high-pressure liquid chromatography (HPLC) system (Agilent Infinity 1260) with a high-precision autosampler (injection error <0.1 μL) and analytical HPLC column ACE (i.d. 2.4 mm, length 250 mm, C18-AR, 5-Å pore size) and separated with isocratic elution with potassium phosphate mobile phase (100 mM, pH 6.0). The rate at each temperature is then obtained by fitting 8 data points and the reported errors are the uncertainty of the fit. Control experiments were performed to determine residual contamination in the commercially purchased ADP, ATP, and AMP stocks.

To assure full substrate saturation with 4 mM MgADP in all enzymatic assays, K_m values of MgADP to Adk was determined with a coupled continuous spectroscopic assay detecting ATP production (*47*) at 25 °C. The K_m for ADP for ANC3 and *B. stearothermophilus* Adk are 510 μM and 126 μM respectively. The discontinuous HPLC assay was used to determine K_m for ADP at high temperatures (Fig. S8).

Eyring plots and the change of heat capacity of activation ($\Delta C_p^{\ddagger}$) fitting

Eyring plots (plotting ln (k_{cat}/T) versus 1/T) were generated using the observed rate constants from temperature dependence kinetics assays. The data were then fitted to equation 1 (Eq. 1) in two scenarios: (1) all three parameters ($\Delta H^{\ddagger}$, $\Delta S^{\ddagger}$ and $\Delta C_p^{\ddagger}$) were allowed to float, (2) $\Delta C_p^{\ddagger}$ was set to 0 (resulting in a linear fit). Subsequent F-tests (p = 0.05) was used to determine which data set required fitting with the inclusion of the parameter $\Delta C_p^{\ddagger}$.

$$\ln\left(\frac{k_{cat}}{T}\right) = \ln\left(\frac{k_B}{h}\right) - \frac{\left[\Delta H_{T_0}^{\ddagger} + \Delta C_p^{\ddagger}\left(T - T_0\right)\right]}{RT} + \frac{\left[\Delta S_{T_0}^{\ddagger} + \Delta C_p^{\ddagger}\ln\left(T / T_0\right)\right]}{R} \qquad \text{(Eq. 1)}$$

where R is gas constant (8.314 $Jmol^{-1}K^{-1}$), k_{cat} is the lid-opening rate constant (s^{-1}), h is Planck's constant (6.626 x 10^{-34} Js), k_B is Boltzmann's constant (1.381 x 10^{-23} JK^{-1}), T is the absolute temperature in Kelvin (K), T_0 is a reference temperature, and $\Delta H_{T_0}^{\ddagger}$ and $\Delta S_{T_0}^{\ddagger}$ are the difference in enthalpy and entropy between the transition state and ground state, respectively at T_0. $\Delta C_p^{\ddagger}$ is defined as the difference in heat capacity between the transition state toward the open state, and the closed state of the enzyme. Note that the gas-phase pre-exponential factor is used, but the value of the pre-exponential factor does not affect $\Delta C_p^{\ddagger}$. The reported errors $\Delta H^{\ddagger}$, $\Delta S^{\ddagger}$ and $\Delta C_p^{\ddagger}$ are the uncertainties of the fit.

Quench-flow kinetics experiments

Pre-steady-state kinetics was measured with a three-syringe rapid quench-flow apparatus RQF-3 (KinTek Corp). 100 μM of protein solution was loaded into one of the syringes, 16 mM of nucleotides (Mg/ADP or AMP + ATP) into the second syringe and quench solution (30% TCA + 6 M HCl mixture) into the third syringe. The reaction was initiated by a simultaneous push of all three syringes by a high-precision servomotor. The required delay between the initial mixing of the reagent and the following quench with acid was achieved by selecting different aging loops. The forward and reverse reactions were initiated by mixture of Adk with Mg/AMP + ATP or Mg/ADP, respectively. The buffer contained 50 mM MOPS, 80 mM KCl, pH 7.0. The desired temperature was controlled with a circulating water bath Isotemp 2150 Nano (Fisher Scientific). The product was neutralized and quantified with HPLC as described above for temperature dependence kinetics assays.

X-ray crystallography

Crystals of ancestral Adks in complex with ADP, AMP*ADP or Ap5A were grown on 96 well plates by using either Hampton Crystal screen HT (Hampton Research, Aliso Viejo, CA, USA) or JBScreen Kinase HTS (Jena Bioscience GmbH, Jena, Germany). The crystals grew by vapor diffusion and sitting drop. For the crystallization experiments, 0.5 μl of the mixture containing 20 mg/ml protein and 20 mM MgADP or 10 mM MgAp5A in 40 mM MOPS pH 7.0, 50 mM NaCl, 2 mM TCEP, were mixed with 0.5 μl mother liquor. The best diffracting crystals were obtained from the following mother liquor solutions: ANC1* Zn*ADP and ANC4*Zn*Mg*Ap5A: 100 mM sodium acetate, pH 4.6, 50 mM magnesium chloride, 2 M ammonium sulfate; ANC3*Zn*Mg*Ap5A: 1.6 M sodium citrate tribasic dihydrate pH 6.5; ANC4*Zn*AMP*ADP: 0.1 M HEPES pH 7.5, 1.4 M sodium citrate tribasic dihydrate. After three weeks of growth at 18 °C, the crystals were flash frozen in liquid nitrogen. All diffraction data were collected at 100 K at the Advanced Light Source beamlines 8.2.1 and 8.2.2 (Berkeley, CA, USA). Data processing was either done with XDS (*48*) and Aimless (*49*) (ANC1 and ANC4) or with Xia2, Distl, Labelit, Mosflm, Pointless, Scala and CCP4 (*49-51*) (ANC3). Prior to

molecular replacement with the program Molrep (*52*), the sequence of the template 1P3J (*29*) was substituted with the respective sequence of the ancestral protein by using the Swiss Model Server (*53*). Refinement and model building was done with Refmac5 (*54*) and COOT (*55, 56*). Table S3 summarizes the data collection/processing statistics and the refinement statistics. Model validation was done with MOLPROBITY and PDB validation.

NMR spectroscopy

[^{1}H-^{15}N]-TROSY-HSQC and ^{15}N CPMG relaxation dispersion experiments (*57*) were performed on an Agilent DD2 600 MHz four-channel spectrometer (at 15, 25, 35, and 45 °C) and a Bruker Avance 800 Mhz (at 15 °C), respectively, each equipped with a triple-resonance cryogenically cooled probe-head. NMR samples contained 1 mM protein and 10 (v/v) % D_2O in 50 mM MOPS, 50 mM NaCl, 2 mM TCEP, pH 7.0. Substrate saturation for the CPMG experiments was achieved with 40 mM Mg/ADP. ^{15}N TROSY CPMG relaxation was measured with a 30 ms constant-time relaxation period, 2 second delay between transients, and refocusing field strengths between 133-1000 Hz collected in an interleaved mode.

NMR data were processed with the NMRPipe/NMRDraw (*58*) software package and analyzed using the program CcpNmr (*59*). Relaxation-dispersion profiles were calculated from PINT(*60*) peak intensities and analyzed with the general Carver-Richards equation (*61*) for two-site exchange with in-house scripts. Intensity uncertainties were estimated from duplicate points. Global fit uncertainties were obtained from a covariance matrix obtained from inversion of the hessian matrix (*62*).

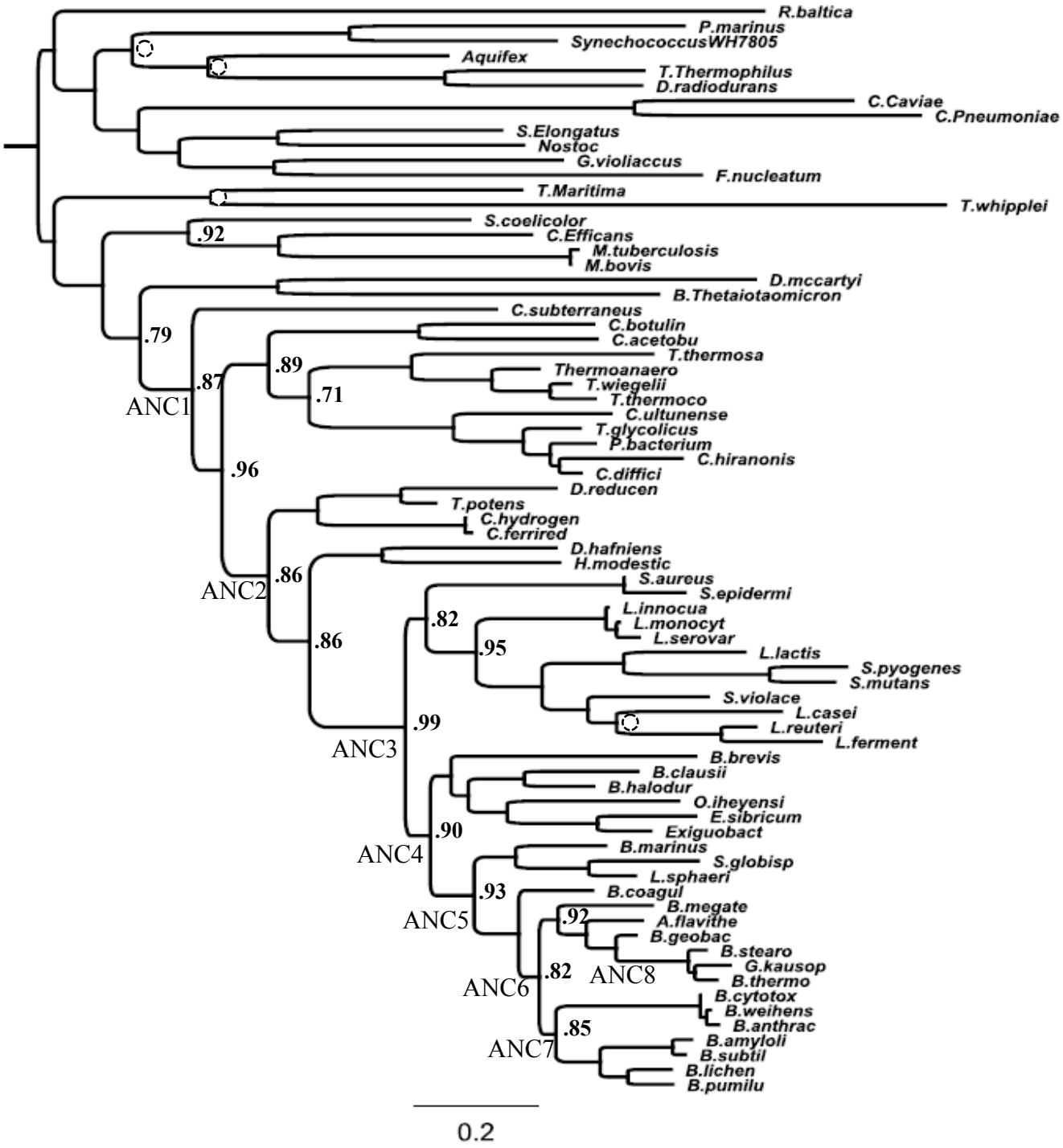

Fig. S1:

Same phylogeny as in Fig. 2 with full clades shown here. Values indicate posterior probabilities of important nodes. All nodes not labeled have probabilities above 0.65 except four nodes denoted with a dotted circle.

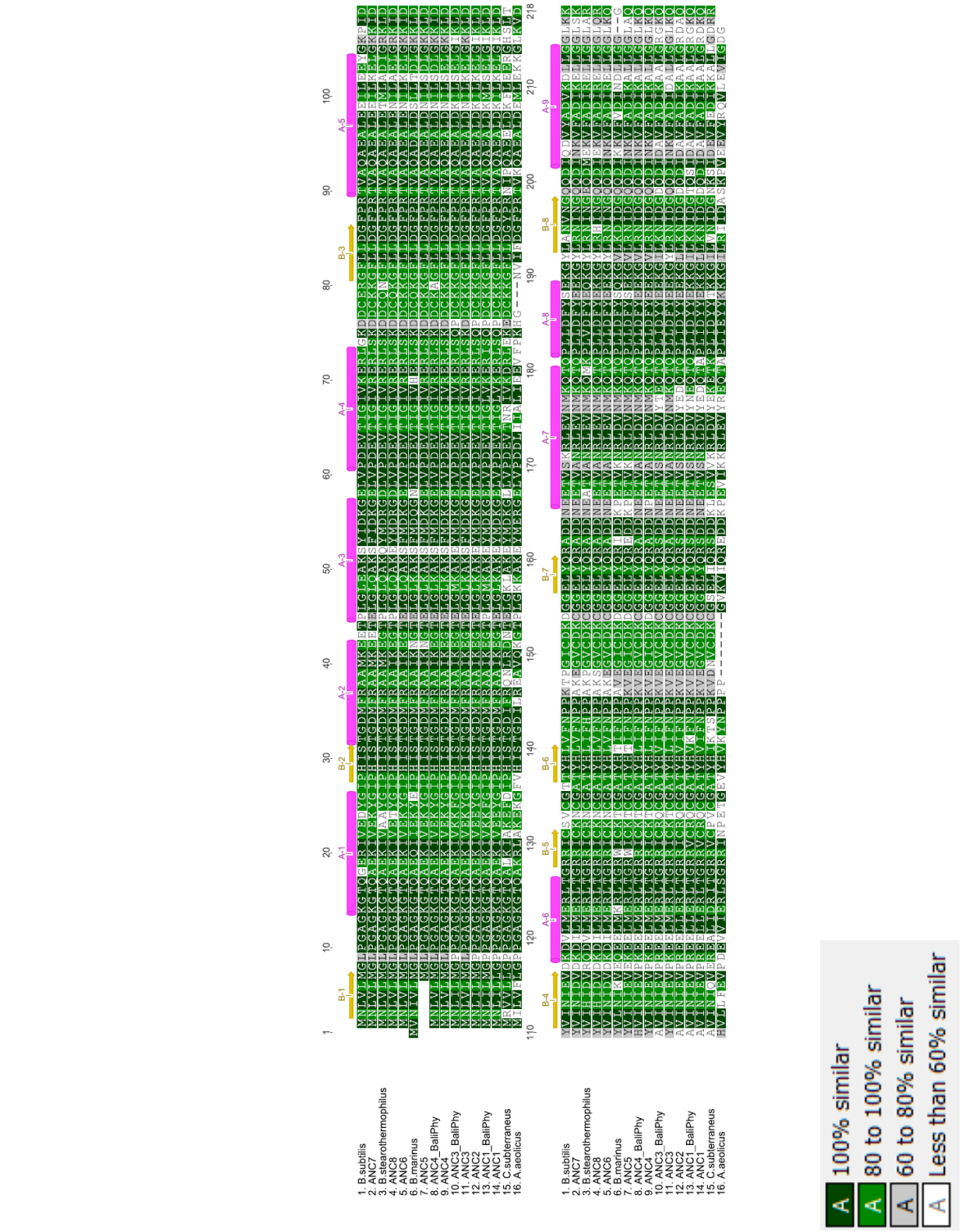

Fig. S2:

Multiple sequence alignment of recreated ancestral Adk enzymes from PAML (*46*) and BAli-Phy (*18*) along with modern sequences characterized in this study, using Adk from *B. subtilis* as reference sequence. Beta sheets are shown as yellow arrows and alpha helices as pink cylinders.

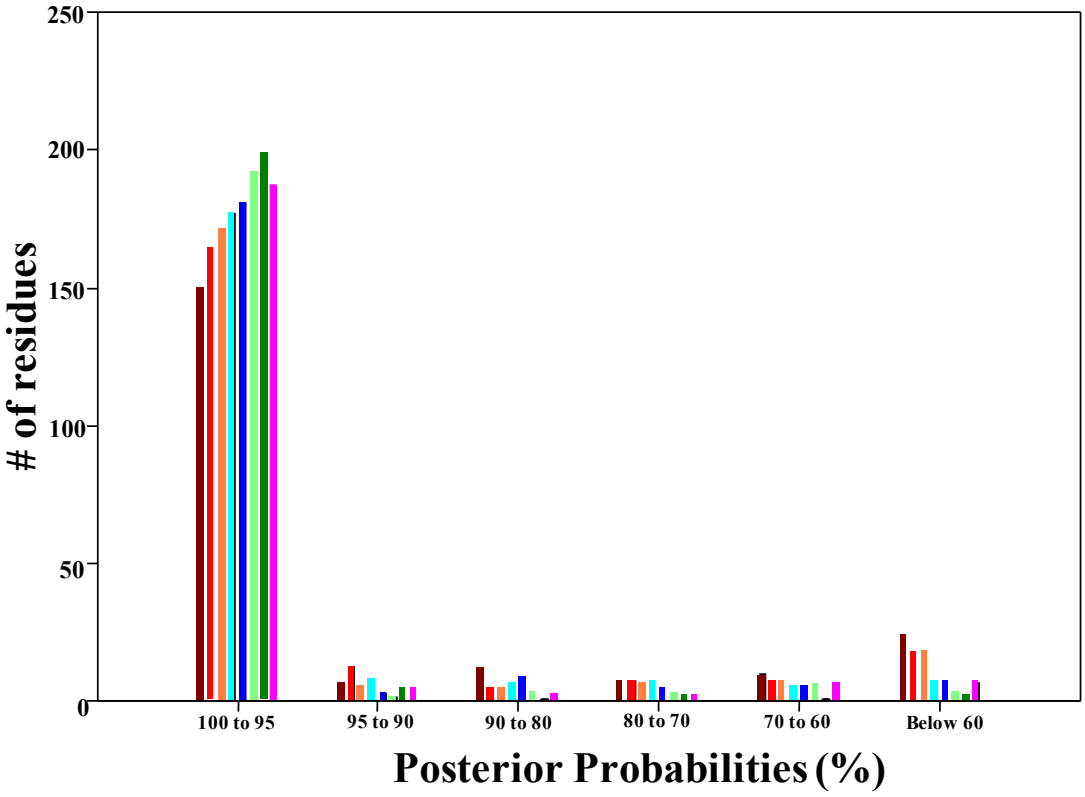

Fig. S3:

Histogram of reconstructed residues binned according to posterior probability of the predicted residue. The color code defined in Fig. 2 is used for the ancestors

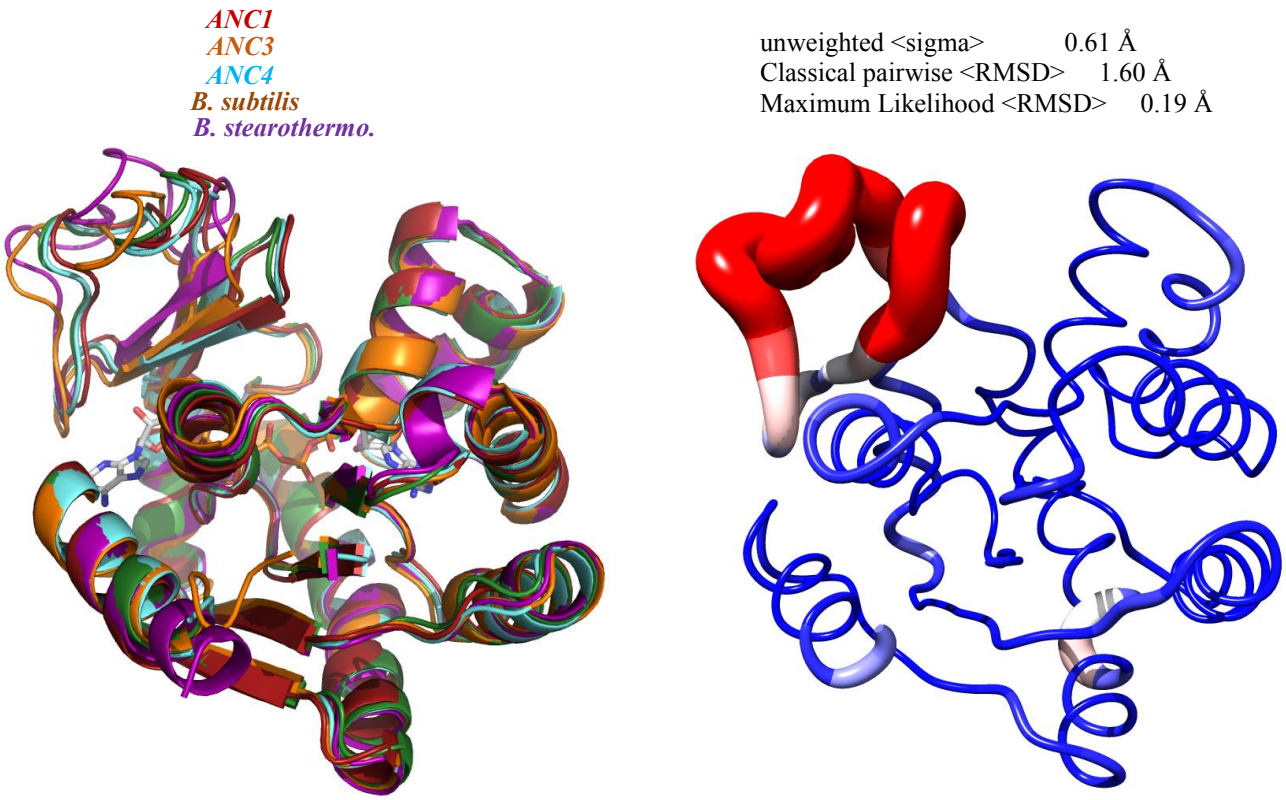

Fig. S4:

(A) Maximum likelihood structural superposition of Adk crystal structures from ANC1, ANC3, ANC4, *B. subtilis* and *B. stearothermophilus* using the THESEUS package (*63, 64*). **(B)** Putty representation of deviation among all structures.

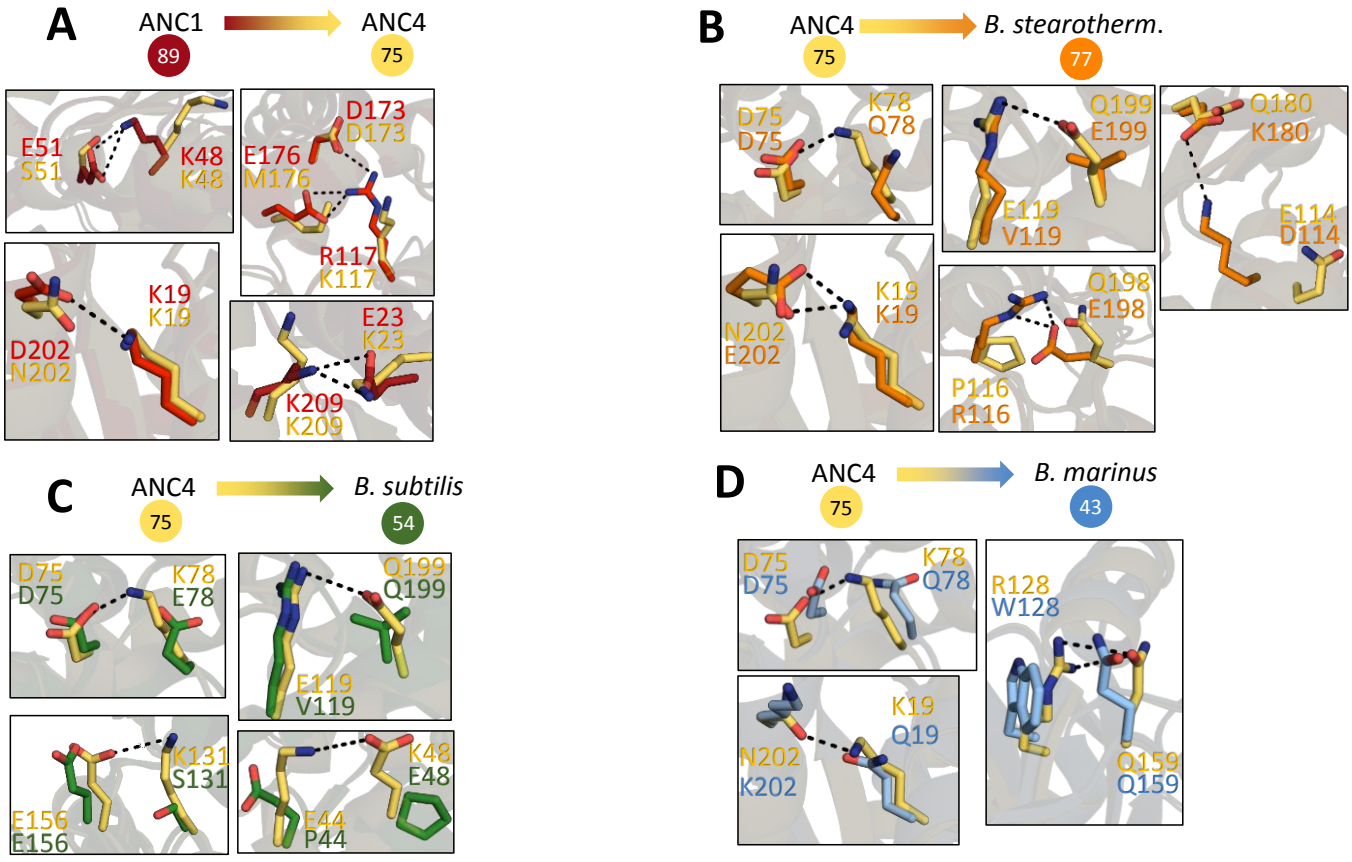

Fig. S5:

Structural analysis of the evolution of thermal stability from **(A)** ANC1 to ANC4, **(B)** ANC4 to *B. stearothermophilus*, **(C)** ANC4 to *B. subtilis* and **(D)** ANC4 to *B. marinus* using published crystal structures (*29, 65*) and the ones solved in this manuscript (5G3Y, 5G3Z, 5G40). **(A)** Four clusters of ion pairs (shown as black dotted lines in ANC1) are lost during the evolutionary pathway from ANC1 to ANC4, potentially explaining the drop of T_m of ANC4 relative to ANC1 by 12 °C (see also experiments in Fig. 2C, D). **(B)** *B. stearothermophilus* evolved from ANC4 via the mesophilic ancestor ANC6. During its evolutionary pathway, the ion-pair D75-K78 as well as the H-bond E119-Q199 are lost, while K19-E202 is reformed and new ion-pairs R116-E198 and D114-K180 evolve. This rebalancing of salt bridges might lead to a similar T_m. **(C)** Four ion pairs are lost during the evolutionary pathway from ANC4 to *B. subtilis* resulting in a drop of T_m by 21 °C. **(D)** Two ion pairs and one H-bond interaction (R128-Q159) are lost during the evolutionary pathway from ANC4 to *B. marinus* possibly playing an important role in the drop of T_m by 31 °C.

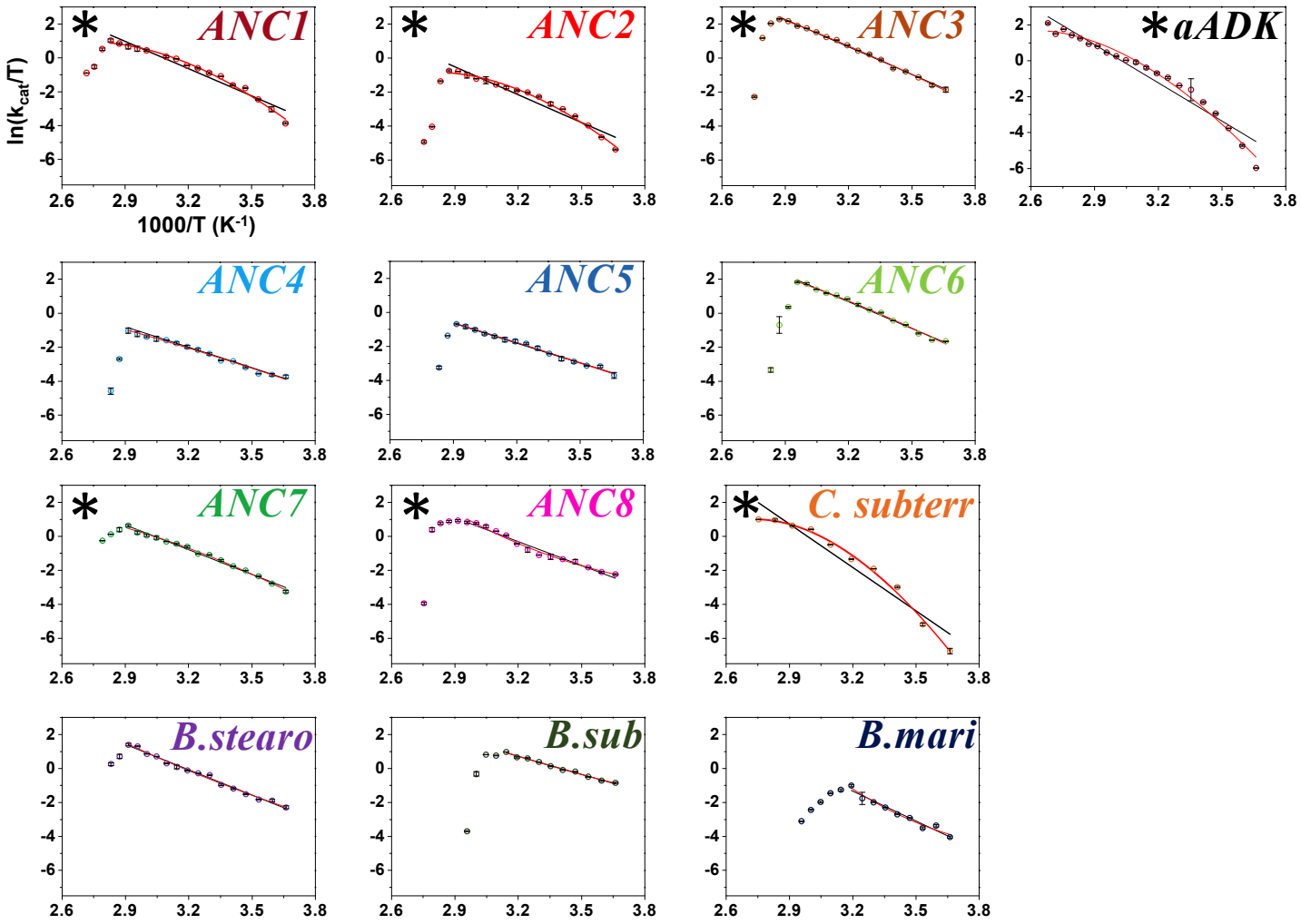

Fig. S6:
Full Eyring plots of all studied Adk enzymes showing the decrease in activity at higher temperatures due to denaturation. Note that this decline (or strong curvature) is there for all enzymes due to general unfolding at temperatures close to T_m, and is much steeper than the shallow positive curvature for ANC1, ANC2, *C. subterraneus* and *A. aeolicus* due to negative $\Delta C_p^{\ddagger}$ of k_{cat}. For fitting of activity data to Eq.1, only data before any unfolding sets in were used (See Fig. S7). Error bars are described in Fig. 3. Black line shows fit with $\Delta C_p^{\ddagger} = 0$. Red line shows fit including $\Delta C_p^{\ddagger}$ as a parameter. Asterisks indicate significant fit enhancements from the inclusion of $\Delta C_p^{\ddagger}$ as a parameter ($p < 0.05$ from F-tests). The temperature dependence of activity shown here unambiguously demonstrates how to differentiate between a decrease in activity with increased temperature caused by denaturation from a true $\Delta C_p^{\ddagger}$ effect on the catalytic step.

We note that in three publications to date from the Arcus lab, a decline in activity at temperatures close to the melting temperatures has been incorrectly interpreted as large negative heat capacity of activation for enzymatic reactions ($\Delta C_p^{\ddagger}$ in the order between 4 to 11 kJ/mol*K) (*66-68*). As shown *(11, 69)*, the measured decline in activity at higher temperatures in *(66-68)* is due to unfolding of the enzyme, in full agreement with our results of a steep decline of activity close to the corresponding T_m.

A

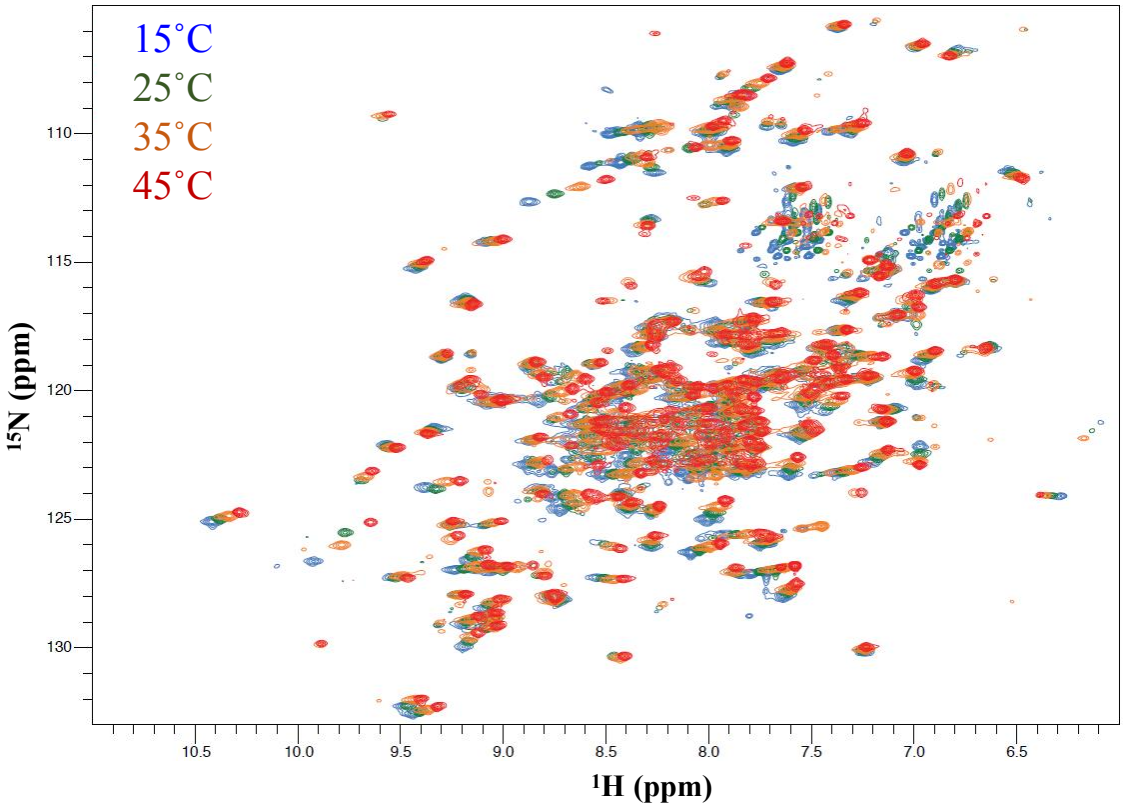

B

Equilibrium Model

$$E_{active} \underset{K_{eq}}{\rightleftharpoons} E_{Inactive}$$

$$k_{cat} = \frac{\frac{k_b T}{h} e^{-\frac{\Delta G^{\ddagger}}{RT}}}{1 + K_{eq}} = \frac{\frac{k_b T}{h} e^{-\frac{\Delta G^{\ddagger}}{RT}}}{1 + e^{\frac{\Delta H_{eq} - T\Delta S_{eq}}{RT}}}$$

$$\ln\left(\frac{k_{cat}}{T}\right) = \ln\left(\frac{k_b}{h}\right) + \frac{\Delta S^{\ddagger}}{R} - \frac{\Delta H^{\ddagger}}{R}\frac{1}{T} - \ln\left(1 + e^{-\frac{\Delta H_{eq} - T\Delta S_{eq}}{RT}}\right)$$

C

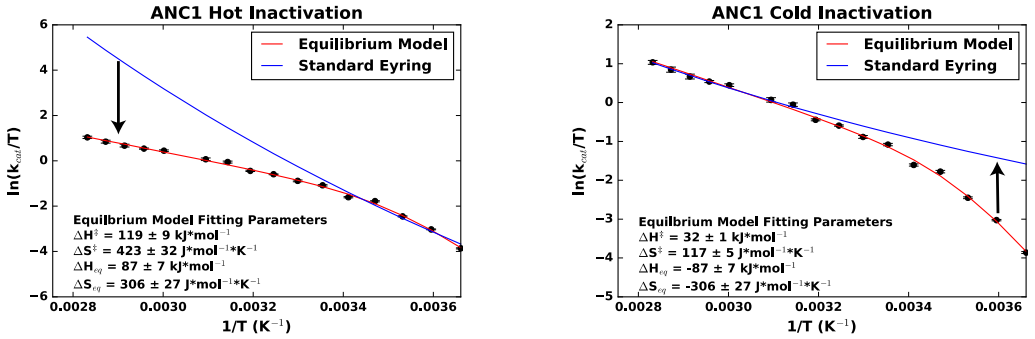

D

Temperature (°C)	ΔG_{eq} Cold Inactivation (J/mol)	ΔG_{eq} Hot Inactivation (J/mol)
0	-3495	3495
5	-2010	2010
10	-525	525
15	960	-960
20	2445	-2445
25	3930	-3930
30	5415	-5415
35	6900	-6900
40	8385	-8385
45	9870	-9870
50	11355	-11355
60	14325	-14325
65	15810	-15810
70	17295	-17295
75	18780	-18780
80	20265	-20265

E

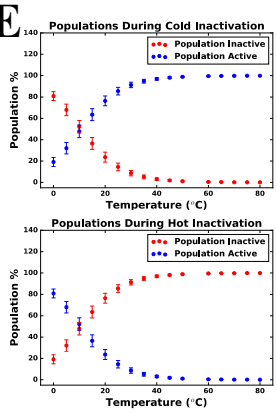

F

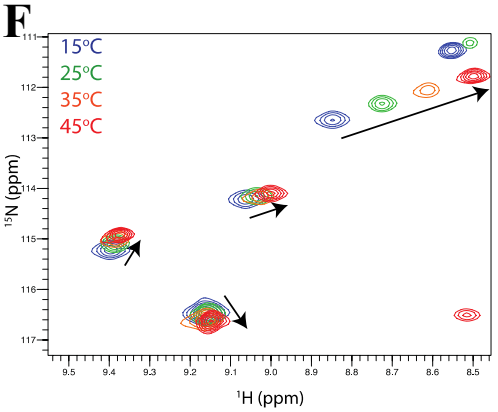

Fig. S7:
Curved Eyring plots in the temperature range fitted are not due to protein denaturation, or temperature dependent inactivation equilibrium. **(A)** ANC1 is fully folded up to 45 °C as measured by NMR ^{1}H ^{15}N HSQC spectra of 1 mM ANC1 at pH 7.0. Chemical shift changes are in agreement with expected linear amide chemical shift changes due to increasing temperature with no sign of denaturation setting in. Eyring plots in the temperature range between 0 °C and 45 °C are used to fit Eq. 1 to determine $\Delta C_p^{\ddagger}$ of k_{cat}. **(B-F)** The equilibrium model of an active-inactive interconversion with a strong temperature dependence of its equilibrium can be ruled out as mechanism for the curved Eyring plots. **(B)** Eyring equation that includes an active-inactive equilibrium of the enzyme with a temperature dependent K_{eq}. **(C)** Fits of Eyring plots of activity data from ANC1 to the equation above for a model of Hot inactivation and Cold inactivation. **(D)** Table of ΔG for this equilibrium at different temperatures. **(E)** Percentage in the inactive and active states at each temperatures illustrating the exponential change with temperature. **(F)** ^{1}H ^{15}N HSQC spectra during enzymatic turnover of ANC1 at different temperatures shows chemical shift changes that are linear with respect to temperature for all residues in the protein, shown here are some representative examples. This is inconsistent with the equilibrium model for which the shifts would be proportional to the population change, hence an exponential dependence on temperature (see E).

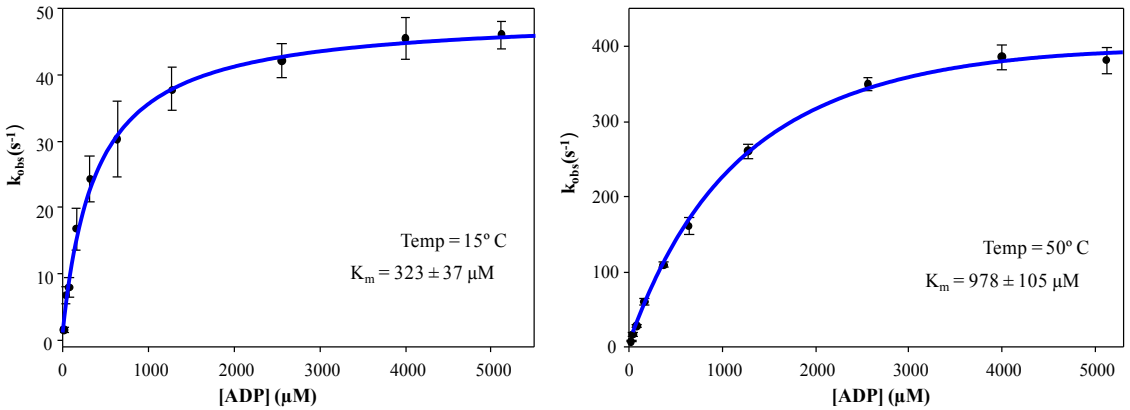

Fig. S8:

Verification that in the temperature range that is used to determine $\Delta C_p^{\ddagger}$ of k_{cat}, the enzyme is indeed under k_{cat} conditions (saturating concentrations for Mg/ADP). Michealis-Menten curve for ANC1 for Mg/ADP shows that while K_m increases with temperature as expected, the enzyme is always at saturating conditions for the performed assays with 4 mM Mg/ADP. Uncertainties are ± SEM from three experiments.

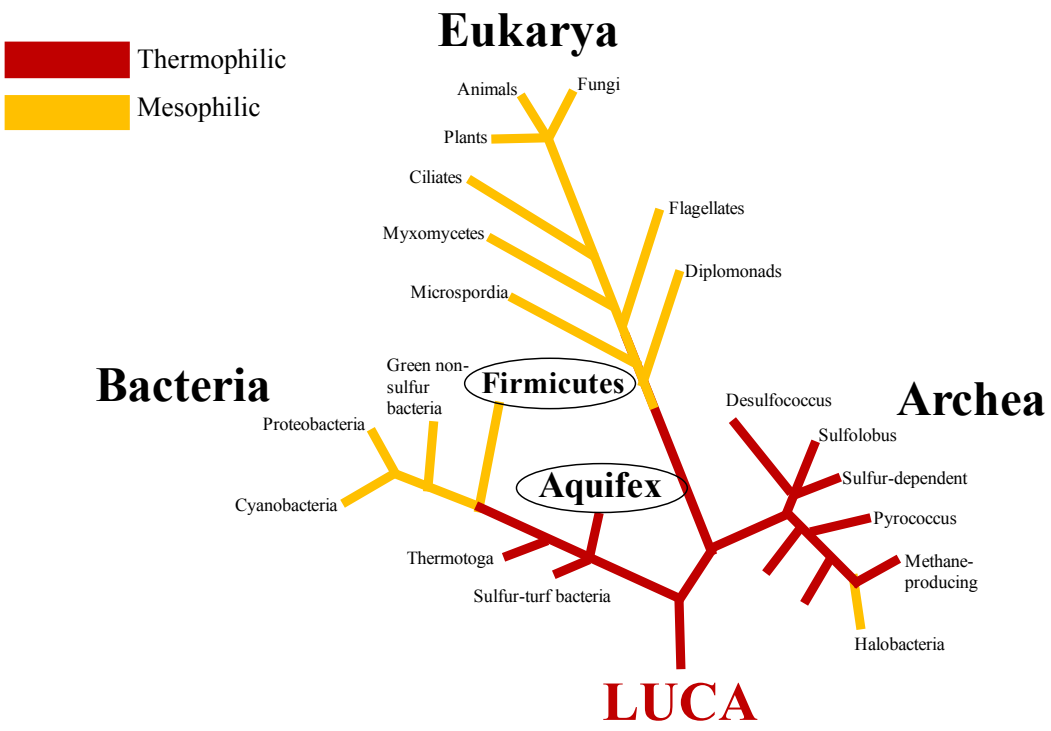

Fig. S9:
Tree adapted from (*70*) that was calculated based on a continuously updated set of 16SRNA sequences. The clades of Firmicutes and *A. aeolicus* used in our study are circled, highlighting that *A. aeolicus* sits near the root of life suggesting it has not moved through a mesophilic ancestor.

	ANC1		ANC3		ANC4	
	PAML	Bali-Phy	PAML	Bali-Phy	PAML	Bali-Phy
Percent Identity	92.2%		84.3%		88.9%	
T_m (˚C)	89.0 ± 0.7	84.7 ± 0.5	77.2 ± 0.1	83.4 ± 0.3	75.8 ± 0.1	75.5 ± 0.1
Max Activity (s^{-1})	1512 ± 80	1134 ± 63	3450 ± 127	2006 ± 110	123 ± 16	527 ± 43
T_{opt} (˚C)	85	85	75	80	70	70
$\Delta C_p^{\ddagger}$ opening (J/mol*K)	-904 ± 99	-821 ± 103	-168 ± 51	-215 ± 81	0	0

Table S1:
Comparison of biophysical parameters for ancestral enzymes constructed by maximum likelihood (ML) and Bayesian methods. Corresponding sequences are shown in Fig. S2. Strikingly, enzymes from the same nodes resurrected from ML or Bayesian methods display very similar biophysical properties within the error of the methods. This result strengthens the validity or our ASR tree and consequently the evolutionary conclusions drawn. This is in contrast to the resurrected ancestors for IPMDH in (*11*) where the authors describe a big error. Uncertainties of T_m are the standard error in the fitted parameter to a 2-state model. Uncertainties of maximum activity are standard errors based on 8 data points at T_{opt} of the ancestral enzymes. Uncertainties of $\Delta C_p^{\ddagger}$ opening are the standard error in fitted parameter of Eq. 1.

	T_m (˚C)	Max Activity (s^{-1})	$\Delta H^{\ddagger}_{opening}$ (15˚C) (kJ/mol)	$\Delta H^{\ddagger}_{opening}$ (50˚C) (kJ/mol)	$\Delta S^{\ddagger}_{opening}$ (15˚C) (J/mol*K)	$\Delta S^{\ddagger}_{opening}$ (50˚C) (J/mol*K)	$\Delta C_p^{\ddagger}$ opening (J/mol*K)
ANC1	89.0 ± 0.7	1512 ± 80	65 ± 6	33 ± 5	17 ± 13	-89 ± 15	-904 ± 99
ANC2	87.4 ± 0.3	994 ± 97	70 ± 6	23 ± 3	23 ± 12	-132 ± 14	-1181 ± 117
ANC3	77.2 ± 0.1	3450 ± 127	53 ± 7	42 ± 4	-14 ± 17	-68 ± 12	-168 ± 51
ANC4	75.8 ± 0.1	123 ± 16	33 ± 1	33 ± 1	-101 ± 2	-101 ± 2	0
ANC5	72.7 ± 0.4	172 ± 10	33 ± 1	33 ± 1	-102 ± 4	-102 ± 4	0
ANC6	65.9 ± 0.1	2119 ± 97	43 ± 1	43 ± 1	48 ± 3	48 ± 3	0
ANC7	72.5 ± 0.3	643 ± 40	48 ± 4	31 ± 4	-41 ± 12	-98 ± 11	-381 ± 145
ANC8	80.6 ± 0.3	862 ± 47	32 ± 6	45 ± 7	-93 ± 14	-53 ± 18	310 ± 152
B. marinus	48.0 ± 0.5	114 ± 12	58 ± 2	58 ± 2	-16 ± 6	-16 ± 6	0
B. subtilis	53.6 ± 0.3	841 ± 7	30 ± 1	30 ± 1	-89 ± 2	-89 ± 2	0
B. stearo.	76.3 ± 0.3	1381 ± 98	42 ± 1	42 ± 1	-57 ± 4	-57 ± 4	0
C. subterr.	88.3 ± 0.4	1117 ± 61	101 ± 5	47 ± 3	161 ± 14	-21 ± 16	-1381 ± 164
A. aeolicus	95.0 ± 0.8	2000 ± 137	90 ± 3	11 ± 1	93 ± 16	-27 ± 6	-910 ± 132

Table S2:
Biophysical parameters for thermal stability and catalytic activity for studied Adk enzymes.
$\Delta C^{\ddagger}_{\text{p opening}}$ values cause the temperature dependence of $\Delta H^{\ddagger}_{\text{opening}}$ and $\Delta S^{\ddagger}_{\text{opening}}$ according to Eq. 1, and we list here the calculated values at a low and high temperature for better visualization of the magnitude of change in these parameters as a function of temperature. Uncertainties are described in Table S1.

	ANC1*Zn *ADP*ADP	ANC3*Zn *Mg*Ap5A	ANC4*Zn *AMP*ADP	ANC4*Zn *Mg*Ap5A
Data collection				
Space group	$P2_12_12_1$	$P2_12_12$	$P12_11$	$P4_32_12$
Cell dimensions				
a, b, c (Å)	46.92, 63.34, 70.46	66.62, 77.44, 38.63	39.05, 70.13, 40.27	73.99, 73.99, 100.78
α, β, γ (°)	90.00, 90.00, 90.00	90.00, 90.00, 90.00	90.00, 103.78, 90.00	90.00, 90.00, 90.00
Resolution (Å)	47.1-1.18 (1.20-1.18)*	77.43-1.89 (1.94-1.89)	39.11-1.69 (1.72-1.69)	59.65-1.54 (1.57-1.54)
R_{merge}	0.057 (0.454)	0.175 (1.304)	0.041 (0.501)	0.056 (1.117)
R_{pim}	0.027 (0.347)	0.073 (0.538)	0.032 (0.366)	0.016 (0.399)
$CC_{1/2}$	0.998 (0.707)	0.993 (0.505)	0.998 (0.741)	1.000 (0.718)
I / σI	15.8 (2.0)	8.6 (2.1)	13.9 (2.0)	23.8 (2.0)
Reflections				
Measured	67513	16553	21392	37185
Unique	2901	1197	1041	1991
Completeness (%)	96.7 (85.0)	100.0 (100.0)	90.2 (87.1)	88.1 (97.1)
Redundancy	6.2 (2.7)	6.7 (6.9)	3.5 (3.4)	13.1 (9.5)
Wilson B Factor ($Å^2$)	9.9	12.5	20.3	18.3
Refinement				
Resolution (Å)	37.70-1.18 (1.21-1.18)	50.50-1.89 (1.94-1.89)	39.11-1.69 (1.73-1.69)	59.65-1.54 (1.58-1.54)
No. reflections	66341	15482	20393	36242
R_{work}/ R_{free}	0.13/0.15 (0.23/0.21)	0.18/0.23 (0.31/0.31)	0.16/0.23 (0.22/0.25)	0.15/0.19 (0.19/0.25)
No. atoms				
Protein	1696	1671	1674	1680
Ligand/Ion	55	59	51	72
Water	261	118	90	185
B-factors ($Å^2$)				
Protein	14.8	20.9	28.0	26.3
Ligand/Ion	9.5	14.2	20.3	20.9
Water	26.2	25.2	36.6	34.5
R.m.s. deviations				
Bond length (Å)	0.011	0.018	0.014	0.013
Bond angles (°)	1.650	2.057	1.818	1.860
PDB ID	5G3Y	5G3Z	5G40	5G41

Table S3:
Data collection and refinement statistics for the 4 solved x-ray structures of ANC1, ANC3 and ANC4.
*Values in parentheses correspond to the highest-resolution shell.

	ANC1	*ANC3*	*ANC4*	*B. subtilis*	*B. stearo.*
Number of Ion Pairs < 4.0 Å	16	14	13	10	13
Distant (>10 residues) Number of Ion Pairs	8	6	5	3	6
Hydrogen Bonds	126	126	122	124	129
Apolar Accessible Area (Å^2)	1749	1844	1778	1687	1790
Polar Accessible Area (Å^2)	1431	1465	1369	1404	1478
Total Accessible Area (Å^2)	3180	3310	3147	3091	3268
Buried Surface Area (Å^2)	7364	7409	7494	7385	7267

Table S4:
What-if analysis (*71*) of solved crystal structures. The only significant differences are in the number of ion pairs.

Construct	ANC1	*C. subterr.*	ANC3	ANC4	*B. marinus*	*B. stearo.*	*B. subtilis*
T_m (°C)	89	79	77	75	43	80	54
PDB	5G3Y	Model after ANC1	5G3Z	5G40	3FB4	1ZIO	1P3J
ion pair	K48	L48	K48	K48	K48	Q48	E48
	E51	E51	S51	S51	S51	Q51	S51
ion pair	R117	R117	K117	K117	Q117	Q117	K117
	D173	D173	D173	D173	D173	E173	E173
	E176	E176	M176	M176	M176	M176	M176
ion pair	K69	K69	R69	R69	H69	R69	K69
	E102	E102	E102	E102	D102	D102	E102
ion pair	K19	K19	K19	K19	Q19	K19	R19
	D202	D202	N202	N202	K202	E202	Q202
ion pair	E23	E23	K23	K23	K23	A23	D23
	K209	K209	D209	K209	N209	R209	K209
Ion-pair	E119	A119	E119	E119	E119	V119	V119
	Q199	K199	Q199	Q199	Q199	Q199	Q199
ion pair	R131	P131	K131	K131	K131	R131	S131
	E156	E156	E156	E156	E156	E156	E156
ion pair	P116	E116	P116	P116	E116	R116	D116
	D198	N198	Q198	Q198	Q198	E198	Q198
ion pair	E114	Q114	E114	E114	K114	D114	E114
	A180	K180	Q180	Q180	Q180	K180	Q180
ion pair	P75	E75	D75	D75	D75	D75	D75
	K78	K78	K78	K78	Q78	Q78	E78
H-bond	R128	R128	R128	R128	W128	R128	R128
	Q159	Q159	Q159	Q159	Q159	Q159	Q159

Table S5:
Comparison of ion-pairs identified from the x-ray structures that possibly are responsible for differences in thermal stability between the studied Adks. Green shaded are cluster forming ion-pairs, while white cells cannot form the ion-pair, either due to loss of acceptor or donor or due to a greater distance than 4 Å. Grey shaded is a tight H-bond cluster found in all Adks but the psychrophile *B. marinus*.

References and Notes

1. A. Clarke, G. J. Morris, F. Fonseca, B. J. Murray, E. Acton, H. C. Price, A low temperature limit for life on Earth. *PLOS ONE* **8**, e66207 (2013). doi:10.1371/journal.pone.0066207 Medline

2. D. A. Cowan, The upper temperature of life—where do we draw the line? *Trends Microbiol.* **12**, 58–60 (2004). doi:10.1016/j.tim.2003.12.002 Medline

3. J. W. Deming, Psychrophiles and polar regions. *Curr. Opin. Microbiol.* **5**, 301–309 (2002). doi:10.1016/S1369-5274(02)00329-6 Medline

4. E. Blöchl, R. Rachel, S. Burggraf, D. Hafenbradl, H. W. Jannasch, K. O. Stetter, Pyrolobus fumarii, gen. and sp. nov., represents a novel group of archaea, extending the upper temperature limit for life to 113 degrees C. *Extremophiles* **1**, 14–21 (1997). doi:10.1007/s007920050010 Medline

5. F. D. Ciccarelli, T. Doerks, C. von Mering, C. J. Creevey, B. Snel, P. Bork, Toward automatic reconstruction of a highly resolved tree of life. *Science* **311**, 1283–1287 (2006). doi:10.1126/science.1123061 Medline

6. L. P. Knauth, D. R. Lowe, High Archean climatic temperature inferred from oxygen isotope geochemistry of cherts in the 3.5 Ga Swaziland Supergroup, South Africa. *Geol. Soc. Am. Bull.* **115**, 566–580 (2003). doi:10.1130/0016-7606(2003)115<0566:HACTIF>2.0.CO;2

7. P. Fralick, J. E. Carter, Neoarchean deep marine paleotemperature: Evidence from turbidite successions. *Precambrian Res.* **191**, 78–84 (2011). doi:10.1016/j.precamres.2011.09.004

8. E. A. Gaucher, S. Govindarajan, O. K. Ganesh, Palaeotemperature trend for Precambrian life inferred from resurrected proteins. *Nature* **451**, 704–707 (2008). doi:10.1038/nature06510 Medline

9. S. Akanuma, Y. Nakajima, S. Yokobori, M. Kimura, N. Nemoto, T. Mase, K. Miyazono, M. Tanokura, A. Yamagishi, Experimental evidence for the thermophilicity of ancestral life. *Proc. Natl. Acad. Sci. U.S.A.* **110**, 11067–11072 (2013). doi:10.1073/pnas.1308215110 Medline

10. V. A. Risso, J. A. Gavira, D. F. Mejia-Carmona, E. A. Gaucher, J. M. Sanchez-Ruiz, Hyperstability and substrate promiscuity in laboratory resurrections of Precambrian β-lactamases. *J. Am. Chem. Soc.* **135**, 2899–2902 (2013). doi:10.1021/ja311630a Medline

11. J. K. Hobbs, C. Shepherd, D. J. Saul, N. J. Demetras, S. Haaning, C. R. Monk, R. M. Daniel, V. L. Arcus, On the origin and evolution of thermophily: Reconstruction of functional precambrian enzymes from ancestors of Bacillus. *Mol. Biol. Evol.* **29**, 825–835 (2012). doi:10.1093/molbev/msr253 Medline

12. R. B. Stockbridge, C. A. Lewis Jr., Y. Yuan, R. Wolfenden, Impact of temperature on the time required for the establishment of primordial biochemistry, and for the evolution of enzymes. *Proc. Natl. Acad. Sci. U.S.A.* **107**, 22102–22105 (2010). doi:10.1073/pnas.1013647107 Medline

13. R. Wolfenden, Primordial chemistry and enzyme evolution in a hot environment. *Cell. Mol. Life Sci.* **71**, 2909–2915 (2014). doi:10.1007/s00018-014-1587-2 Medline

14. M. J. Harms, J. W. Thornton, Evolutionary biochemistry: Revealing the historical and physical causes of protein properties. *Nat. Rev. Genet.* **14**, 559–571 (2013). doi:10.1038/nrg3540 Medline

15. R. Couñago, Y. Shamoo, Gene replacement of adenylate kinase in the gram-positive thermophile Geobacillus stearothermophilus disrupts adenine nucleotide homeostasis and reduces cell viability. *Extremophiles* **9**, 135–144 (2005). doi:10.1007/s00792-004-0428-x Medline

16. R. Couñago, S. Chen, Y. Shamoo, In vivo molecular evolution reveals biophysical origins of organismal fitness. *Mol. Cell* **22**, 441–449 (2006). doi:10.1016/j.molcel.2006.04.012 Medline

17. A. Moreno-Letelier, G. Olmedo-Alvarez, L. E. Eguiarte, V. Souza, Divergence and phylogeny of Firmicutes from the Cuatro Ciénegas Basin, Mexico: A window to an ancient ocean. *Astrobiology* **12**, 674–684 (2012). doi:10.1089/ast.2011.0685 Medline

18. B. D. Redelings, M. A. Suchard, Joint Bayesian estimation of alignment and phylogeny. *Syst. Biol.* **54**, 401–418 (2005). doi:10.1080/10635150590947041 Medline

19. F. U. Battistuzzi, A. Feijao, S. B. Hedges, A genomic timescale of prokaryote evolution: Insights into the origin of methanogenesis, phototrophy, and the colonization of land. *BMC Evol. Biol.* **4**, 44 (2004). doi:10.1186/1471-2148-4-44 Medline

20. P. D. Williams, D. D. Pollock, B. P. Blackburne, R. A. Goldstein, Assessing the accuracy of ancestral protein reconstruction methods. *PLOS Comput. Biol.* **2**, e69 (2006). doi:10.1371/journal.pcbi.0020069 Medline

21. A. Case, R. L. Stein, Mechanistic origins of the substrate selectivity of serine proteases. *Biochemistry* **42**, 3335–3348 (2003). doi:10.1021/bi020668l Medline

22. S. J. Kerns, R. V. Agafonov, Y.-J. Cho, F. Pontiggia, R. Otten, D. V. Pachov, S. Kutter, L. A. Phung, P. N. Murphy, V. Thai, T. Alber, M. F. Hagan, D. Kern, The energy landscape of adenylate kinase during catalysis. *Nat. Struct. Mol. Biol.* **22**, 124–131 (2015). doi:10.1038/nsmb.2941 Medline

23. M. Oliveberg, Y. J. Tan, A. R. Fersht, Negative activation enthalpies in the kinetics of protein folding. *Proc. Natl. Acad. Sci. U.S.A.* **92**, 8926–8929 (1995). doi:10.1073/pnas.92.19.8926 Medline

24. G. A. Petsko, Structural basis of thermostability in hyperthermophilic proteins, or “there’s more than one way to skin a cat”. *Methods Enzymol.* **334**, 469–478 (2001). doi:10.1016/S0076-6879(01)34486-5 Medline

25. D. R. Zeigler, The Geobacillus paradox: Why is a thermophilic bacterial genus so prevalent on a mesophilic planet? *Microbiology* **160**, 1–11 (2014). doi:10.1099/mic.0.071696-0 Medline

26. R. A. Goldstein, The evolution and evolutionary consequences of marginal thermostability in proteins. *Proteins* **79**, 1396–1407 (2011). doi:10.1002/prot.22964 Medline

27. E. Bornberg-Bauer, H. S. Chan, Modeling evolutionary landscapes: Mutational stability, topology, and superfunnels in sequence space. *Proc. Natl. Acad. Sci. U.S.A.* **96**, 10689–10694 (1999). doi:10.1073/pnas.96.19.10689 Medline

28. V. A. Risso, J. A. Gavira, D. F. Mejia-Carmona, E. A. Gaucher, J. M. Sanchez-Ruiz; J. A. G. Valeria A. Risso, Hyperstability and substrate promiscuity in laboratory resurrections of Precambrian β-lactamases. *J. Am. Chem. Soc.* **135**, 2899–2902 (2013). doi:10.1021/ja311630a Medline

29. E. Bae, G. N. Phillips Jr., Structures and analysis of highly homologous psychrophilic, mesophilic, and thermophilic adenylate kinases. *J. Biol. Chem.* **279**, 28202–28208 (2004). doi:10.1074/jbc.M401865200 Medline

30. N. V. Prabhu, K. A. Sharp, Heat capacity in proteins. *Annu. Rev. Phys. Chem.* **56**, 521–548 (2005). doi:10.1146/annurev.physchem.56.092503.141202 Medline

31. C. Canepa, On the curvature in logarithmic plots of rate coefficients for chemical reactions. *Chem. Cent. J.* **5**, 22 (2011). doi:10.1186/1752-153X-5-22 Medline

32. R. Nussinov, P. G. Wolynes, A second molecular biology revolution? The energy landscapes of biomolecular function. *Phys. Chem. Chem. Phys.* **16**, 6321–6322 (2014). doi:10.1039/c4cp90027h Medline

33. P. G. Wolynes, W. A. Eaton, A. R. Fersht, Chemical physics of protein folding. *Proc. Natl. Acad. Sci. U.S.A.* **109**, 17770–17771 (2012). doi:10.1073/pnas.1215733109 Medline

34. R. B. Stockbridge, R. Wolfenden, The intrinsic reactivity of ATP and the catalytic proficiencies of kinases acting on glucose, N-acetylgalactosamine, and homoserine: A thermodynamic analysis. *J. Biol. Chem.* **284**, 22747–22757 (2009). doi:10.1074/jbc.M109.017806 Medline

35. G. Holtmann, E. Bremer, Thermoprotection of Bacillus subtilis by exogenously provided glycine betaine and structurally related compatible solutes: Involvement of Opu transporters. *J. Bacteriol.* **186**, 1683–1693 (2004). doi:10.1128/JB.186.6.1683-1693.2004 Medline

36. D. S. Nichols, P. D. Nichols, T. A. McMeekin, Ecology and physiology of psychrophilic bacteria from Antarctic saline lakes and ice-sea. *Sci. Prog.* **78**, 311–348 (1995).

37. T. N. Nazina, T. P. Tourova, A. B. Poltaraus, E. V. Novikova, A. A. Grigoryan, A. E. Ivanova, A. M. Lysenko, V. V. Petrunyaka, G. A. Osipov, S. S. Belyaev, M. V. Ivanov, Taxonomic study of aerobic thermophilic bacilli: Descriptions of Geobacillus subterraneus gen. nov., sp. nov. and Geobacillus uzenensis sp. nov. from petroleum reservoirs and transfer of Bacillus stearothermophilus, Bacillus thermocatenulatus, Bacillus thermoleovorans, Bacillus kaustophilus, Bacillus thermodenitrificans to Geobacillus as the new combinations G. stearothermophilus, G. th. *Int. J. Syst. Evol. Microbiol.* **51**, 433–446 (2001). doi:10.1099/00207713-51-2-433 Medline

38. R. Huber, K. O. Stetter, Discovery of hyperthermophilic microorganisms. *Methods Enzymol.* **330**, 11–24 (2001). doi:10.1016/S0076-6879(01)30367-1 Medline

39. S. F. Altschul, W. Gish, W. Miller, E. W. Myers, D. J. Lipman, Basic local alignment search tool. *J. Mol. Biol.* **215**, 403–410 (1990). doi:10.1016/S0022-2836(05)80360-2 Medline

40. K. Katoh, K. Misawa, K. Kuma, T. Miyata, MAFFT: A novel method for rapid multiple sequence alignment based on fast Fourier transform. *Nucleic Acids Res.* **30**, 3059–3066 (2002). doi:10.1093/nar/gkf436 Medline

41. B. D. Redelings, M. A. Suchard, Incorporating indel information into phylogeny estimation for rapidly emerging pathogens. *BMC Evol. Biol.* **7**, 40 (2007). doi:10.1186/1471-2148-7-40 Medline

42. S. Q. Le, O. Gascuel, An improved general amino acid replacement matrix. *Mol. Biol. Evol.* **25**, 1307–1320 (2008). doi:10.1093/molbev/msn067 Medline

43. S. Guindon, J. F. Dufayard, V. Lefort, M. Anisimova, W. Hordijk, O. Gascuel, New algorithms and methods to estimate maximum-likelihood phylogenies: Assessing the performance of PhyML 3.0. *Syst. Biol.* **59**, 307–321 (2010). doi:10.1093/sysbio/syq010 Medline

44. J. P. Huelsenbeck, F. Ronquist, MRBAYES: Bayesian inference of phylogenetic trees. *Bioinformatics* **17**, 754–755 (2001). doi:10.1093/bioinformatics/17.8.754 Medline

45. S. P. Brooks, A. Gelman, General methods for monitoring convergence of iterative simulations. *J. Comput. Graph. Stat.* **7**, 434–455 (1998).

46. Z. Yang, PAML 4: Phylogenetic analysis by maximum likelihood. *Mol. Biol. Evol.* **24**, 1586–1591 (2007). doi:10.1093/molbev/msm088 Medline

47. F. Fan, K. V. Wood, Bioluminescent assays for high-throughput screening. *Assay Drug Dev. Technol.* **5**, 127–136 (2007). doi:10.1089/adt.2006.053 Medline

48. W. Kabsch, Xds. *Acta Crystallogr. D Biol. Crystallogr.* **66**, 125–132 (2010). doi:10.1107/S0907444909047337 Medline

49. P. Evans, Scaling and assessment of data quality. *Acta Crystallogr. D Biol. Crystallogr.* **62**, 72–82 (2006). doi:10.1107/S0907444905036693 Medline

50. N. K. Sauter, R. W. Grosse-Kunstleve, P. D. Adams, Robust indexing for automatic data collection. *J. Appl. Crystallogr.* **37**, 399–409 (2004). doi:10.1107/S0021889804005874 Medline

51. Z. Zhang, N. K. Sauter, H. van den Bedem, G. Snell, A. M. Deacon, Automated diffraction image analysis and spot searching for high-throughput crystal screening. *J. Appl. Cryst.* **39**, 112–119 (2006). doi:10.1107/S0021889805040677

52. A. Vagin, A. Teplyakov, MOLREP: An automated program for molecular replacement. *J. Appl. Cryst.* **30**, 1022–1025 (1997). doi:10.1107/S0021889897006766

53. K. Arnold, L. Bordoli, J. Kopp, T. Schwede, The SWISS-MODEL workspace: A web-based environment for protein structure homology modelling. *Bioinformatics* **22**, 195–201 (2006). doi:10.1093/bioinformatics/bti770 Medline

54. G. N. Murshudov, P. Skubák, A. A. Lebedev, N. S. Pannu, R. A. Steiner, R. A. Nicholls, M. D. Winn, F. Long, A. A. Vagin, REFMAC5 for the refinement of macromolecular crystal structures. *Acta Crystallogr. D Biol. Crystallogr.* **67**, 355–367 (2011). doi:10.1107/S0907444911001314 Medline

55. P. Emsley, K. Cowtan, Coot: Model-building tools for molecular graphics. *Acta Crystallogr. D Biol. Crystallogr.* **60**, 2126–2132 (2004). doi:10.1107/S0907444904019158 Medline

56. P. Emsley, B. Lohkamp, W. G. Scott, K. Cowtan, Features and development of Coot. *Acta Crystallogr. D Biol. Crystallogr.* **66**, 486–501 (2010). doi:10.1107/S0907444910007493 Medline

57. J. P. Loria, M. Rance, A. G. Palmer 3rd, A TROSY CPMG sequence for characterizing chemical exchange in large proteins. *J. Biomol. NMR* **15**, 151–155 (1999). doi:10.1023/A:1008355631073 Medline

58. F. Delaglio, S. Grzesiek, G. W. Vuister, G. Zhu, J. Pfeifer, A. Bax, NMRPipe: A multidimensional spectral processing system based on UNIX pipes. *J. Biomol. NMR* **6**, 277–293 (1995). doi:10.1007/BF00197809 Medline

59. W. F. Vranken, W. Boucher, T. J. Stevens, R. H. Fogh, A. Pajon, M. Llinas, E. L. Ulrich, J. L. Markley, J. Ionides, E. D. Laue, The CCPN data model for NMR spectroscopy: Development of a software pipeline. *Proteins* **59**, 687–696 (2005). doi:10.1002/prot.20449 Medline

60. A. Ahlner, M. Carlsson, B. H. Jonsson, P. Lundström, PINT: A software for integration of peak volumes and extraction of relaxation rates. *J. Biomol. NMR* **56**, 191–202 (2013). doi:10.1007/s10858-013-9737-7 Medline

61. J. P. Carver, R. E. Richards, A general two-site solution for the chemical exchange produced dependence of T2 upon the carr-Purcell pulse separation. *J. Magn. Reson.* **6**, 89–105 (1972).

62. W. H. Press, S. A. Teukolsky, W. T. Vetterling, B. P. Flannery, *Numerical Recipes 3rd Edition: The Art of Scientific Computing*. (Cambridge University Press, 2007), pp. 1256.

63. D. L. Theobald, P. A. Steindel, Optimal simultaneous superpositioning of multiple structures with missing data. *Bioinformatics* **28**, 1972–1979 (2012). doi:10.1093/bioinformatics/bts243 Medline

64. D. L. Theobald, D. S. Wuttke, Accurate structural correlations from maximum likelihood superpositions. *PLOS Comput. Biol.* **4**, e43 (2008). doi:10.1371/journal.pcbi.0040043 Medline

65. M. Davlieva, Y. Shamoo, Structure and biochemical characterization of an adenylate kinase originating from the psychrophilic organism Marinibacillus marinus. *Acta Crystallogr. Sect. F Struct. Biol. Cryst. Commun.* **65**, 751–756 (2009). doi:10.1107/S1744309109024348 Medline

66. V. L. Arcus, C. R. Pudney, Change in heat capacity accurately predicts vibrational coupling in enzyme catalyzed reactions. *FEBS Lett.* **589**, 2200–2206 (2015). doi:10.1016/j.febslet.2015.06.042 Medline

67. J. K. Hobbs, W. Jiao, A. D. Easter, E. J. Parker, L. A. Schipper, V. L. Arcus, Change in heat capacity for enzyme catalysis determines temperature dependence of enzyme catalyzed rates. *ACS Chem. Biol.* **8**, 2388–2393 (2013). doi:10.1021/cb4005029 Medline

68. V. L. Arcus, E. J. Prentice, J. K. Hobbs, A. J. Mulholland, M. W. Van der Kamp, C. R. Pudney, E. J. Parker, L. A. Schipper, On the Temperature Dependence of Enzyme-Catalyzed Rates. *Biochemistry* **55**, 1681–1688 (2016). doi:10.1021/acs.biochem.5b01094 Medline

69. Y. V. Griko, G. I. Makhatadze, P. L. Privalov, R. W. Hartley, Thermodynamics of barnase unfolding. *Protein Sci.* **3**, 669–676 (1994). doi:10.1002/pro.5560030414 Medline

70. R. Munoz, P. Yarza, W. Ludwig, J. Euzéby, R. Amann, K.-H. Schleifer, F. O. Glöckner, R. Rosselló-Móra, Release LTPs104 of the All-Species Living Tree. *Syst. Appl. Microbiol.* **34**, 169–170 (2011). doi:10.1016/j.syapm.2011.03.001 Medline

71. G. Vriend, WHAT IF: A molecular modeling and drug design program. *J. Mol. Graph.* **8**, 52–56, 29 (1990). Medline